

Molecular and anatomical organization of the dorsal raphe nucleus

Kee Wui Huang¹, Nicole E. Ochandarena¹, Adrienne C. Philson¹, Minsuk Hyun¹, Jaclyn E. Birnbaum¹, Marcelo Cicconet², and Bernardo L. Sabatini¹

¹ Howard Hughes Medical Institute, Department of Neurobiology, Harvard Medical School, Boston, MA 02115, USA.

² Image and Data Analysis Core, Harvard Medical School, Boston, MA 02115, USA

Correspondence: bsabatini@hms.harvard.edu

ABSTRACT

1 The dorsal raphe nucleus (DRN) is an important source of neuromodulators in the brain and
 2 has been implicated in a wide variety of behavioral and neurological disorders. Although
 3 mostly studied as a source of serotonin, the DRN is comprised of multiple cell types that are
 4 subdivided into distinct anatomical subregions. However, the complex and incompletely
 5 characterized cellular organization of the DRN has impeded efforts to investigate the distinct
 6 circuit and behavioral functions of its subdomains. Here we used high-throughput single-cell
 7 RNA sequencing with *in situ* hybridization and viral tracing to develop a map of transcriptional
 8 and spatial profiles of cells in and around the mouse DRN. Our studies reveal the molecular
 9 and spatial organization of multiple neuron subtypes that are the cellular bases of functionally
 10 and anatomically distinct serotonergic subsystems, and provide a resource for the design of
 11 strategies for further dissection of these subsystems and their diverse functions.

INTRODUCTION

The dorsal raphe nucleus (DRN) is a major source of neuromodulators in the central nervous system, and is the largest of the serotonergic nuclei, containing approximately a third of all serotonergic neurons (5-HT neurons) in the brain (Hornung, 2010). DRN 5-HT neurons send highly divergent projections that target many functionally distinct brain regions (Azmitia and Segal, 1978; Muzerelle et al., 2016; Vertes, 1991). Concordantly, diverse and at times conflicting functions have been proposed for DRN 5-HT neurons, including arousal (Monti, 2010), motor facilitation (Jacobs and Fornal, 1997), behavioral inhibition (Miyazaki et al., 2012), cognitive flexibility (Matias et al., 2017), value representation (Bromberg-Martin et al., 2010; Cohen et al., 2015; Hayashi et al., 2015; Li et al., 2016), motor learning (Kawashima et al., 2016), mood (Cools et al., 2008), and regulation of social interactions (Dölen et al., 2013; Niederkofler et al., 2016). Changes in DRN 5-HT neuron function have been implicated in various neuropsychiatric diseases, including major depressive disorder, bipolar disorder, schizophrenia, and obsessive-compulsive disorder, as well as movement disorders such as Parkinson's Disease (Huot et al., 2011; Mahmood and Silverstone, 2001; Politis and Niccolini, 2014; Vaswani et al., 2003). Serotonergic signaling pathways are also targets of widely-used therapeutic drugs, such as selective serotonin reuptake inhibitors (SSRIs) and atypical antipsychotics (Meltzer and Massey, 2011; Vaswani et al., 2003). However many of these drugs can acutely induce adverse side effects including anxiety and increased risk of suicidal behaviors (Ferguson, 2001; Gartlehner et al., 2011; Vaswani et al., 2003). This suggests these drugs affect multiple 5-HT pathways with distinct and contrasting effects on behavior and highlights the need for new approaches to target specific 5-HT neurons and their outputs (Marcinkiewicz et al., 2016; Urban et al., 2016). Understanding of the organization of the DRN

and 5-HT neurons in functionally distinct subsystems may help explain conflicting conclusions for the role of serotonin in the etiology of mental disorders.

Neurons in the DRN are neurochemically and anatomically diverse such that only 30 to 50% are serotonergic, and many release other neurotransmitters including GABA, glutamate, dopamine (DA), nitric oxide, and a variety of peptides (Fu et al., 2010). Some DRN neurons co-express genes that are traditionally used as markers for different neuronal cell types based on their neurotransmitter usage (e.g. *Gad1*, *Gad2*, *Slc17a6*, and *Slc17a8*) (Fu et al., 2010; Okaty et al., 2015). This presents a major challenge to attempts at separating cell types in the DRN using many genetic driver lines, which will label mixed populations in the DRN that have overlapping expression of these “canonical” marker genes. Furthermore, these distinct neuronal cell types are spatially intermingled within the DRN and are difficult to separate anatomically.

Even bona fide DRN 5-HT neurons are molecularly, anatomically, and physiologically heterogeneous. Cytoarchitecturally, the DRN contains the 5-HT neuron clusters B6 and B7 (Dahlström and Fuxe, 1964; Hornung, 2010), and is further divided into subregions along all three major anatomical axes (Hale and Lowry, 2011). Although these subregions can be roughly defined by the spatial clustering of 5-HT neurons, the density of 5-HT neurons varies gradually between the subregions preventing the delineation of clear boundaries. Although DRN 5-HT neurons share a common developmental lineage (Deneris and Gaspar, 2018; Jensen et al., 2008), DRN 5-HT neurons in different subregions express different G protein-coupled receptors and vesicular transporters, suggesting spatial clustering of functionally

specialized neurons (Calizo et al., 2011; Fernandez et al., 2015; Lowry et al., 2000; Templin et al., 2012). Nevertheless, these anatomical subregions fail to capture many features of 5-HT neurons, as most of the variation does not show subregional specificity. Additionally, DRN 5-HT neurons vary in their axonal projection patterns, and the spatial distributions of these projection-defined subpopulations are broad and do not map cleanly to DRN subregions. This likely arises, in part, from the extensive collateralization of axons from individual 5-HT neurons (Gagnon and Parent, 2014; Waselus et al., 2011) – different 5-HT neurons are therefore likely to have overlapping axonal projection fields, even if they target distinct sets of regions to serve separate functions.

The heterogeneity of 5-HT neurons suggests that they may be organized into distinct subsystems. However, there is no consensus on the definition of these subsystems and only an incomplete understanding of correspondences between anatomically, molecularly, and functionally defined 5-HT neuron subtypes. Functional differences exist between projection-defined subpopulations of DRN 5-HT neurons (Ren et al., 2018), but it is unknown if these subpopulations map onto molecularly defined subtypes. Furthermore an unbiased census of DRN cell types and subtypes of 5-HT neurons is lacking, and presents a major obstacle in achieving a unified understanding of the diverse functions performed by these neurons.

Here we dissect the cellular composition of the DRN and relate molecular profiles of cell types to anatomical features. We used high-throughput single-cell RNA sequencing (scRNA-seq) to survey the cell types in and around the DRN and identified at least 5 distinct subtypes of 5-HT neurons, in addition to uncovering organizational principles for both neuronal and non-neuronal

cell types based on gene expression profiles. Spatial information from *in situ* hybridization imaging datasets allowed us to infer the anatomical distribution of these DRN 5-HT neuron subtypes within the DRN. Molecularly defined subtypes of DRN 5-HT neurons are found in overlapping but different sets of anatomical subregions that do not match the spatial distribution of projection-defined subpopulations. Using viral retrograde tracing and multiplexed *in situ* hybridization, we characterized the expression of subtype-enriched genes in projection-defined neuronal subpopulations and found that the striatal-projecting 5-HT neuron subpopulation is a heterogeneous group comprised of at least 2 distinct molecular subtypes. Additionally, we defined a DRN 5-HT neuron subtype that is well-positioned to modulate basal ganglia circuits, based on its molecular and anatomical features. Our findings validate the feasibility of intersectional approaches to achieve the molecular and spatial specificity required to access distinct 5-HT neuron subsystems *in vivo*, and provide a resource to aid in the design of experimental strategies for the functional dissection of diverse DRN cell types and circuits.

RESULTS

Cell type composition of the DRN by transcriptomic profiling

To survey the cell type composition of the DRN, we used the droplet-based inDrop platform (Klein et al., 2015; Zilionis et al., 2017) to perform transcriptomic profiling with single-cell resolution (Fig. 1A). The DRN and surrounding areas were dissected from acute coronal brain sections spanning the rostro-caudal extent of the DRN, and dissociated cell suspensions were prepared by digesting the dissected tissue in a protease cocktail containing inhibitors of neural activity, transcription, and translation to reduce the effects of the dissociation procedure on gene expression (Hrvatin et al., 2018). Cells were sequenced to an average read depth of 48,805 reads per cell (median = 31,286 reads), and low-quality cells were removed prior to clustering (see Methods). Aligned reads were filtered using unique molecular identifiers (UMIs) and quantified as UMI filtered mapped read (UMIFM) counts. Clustering using a graph-based algorithm and a shared-nearest-neighbors distance metric grouped yielded 17 major clusters (Fig. 1B). These major clusters were identified and assigned to cell classes based their expression of previously-described marker gene combinations that were extensive cross-referenced with published datasets (Marques et al., 2016; Okaty et al., 2015; Poulin et al., 2014; Saunders et al., 2018; Vanlandewijck et al., 2018; Zeisel et al., 2018) (Fig. 1C, Table S1). Smaller clusters containing putative doublets were identified based on co-expression of marker genes from different cell types and were removed manually. The processed dataset contained 39,411 cells from 8 mice (4 male and 4 female, age range 8-10 weeks) with a median UMIFM count of 2333 counts per cell (min. = 548, max. = 17976, IQR = 1903) and median gene detection rate of 1034 genes per cell (min. = 216, max. = 5765, IQR = 693). Cells

from male and female mice were pooled for analysis as no major transcriptional sex differences were observed (Fig. S1).

The majority of cells in the dataset were non-neuronal cells that included astrocytes, oligodendrocyte precursor cells (or polydendrocytes), differentiating and mature oligodendrocytes, ependymal cells of the cerebral aqueduct, lymphocytes, microglia, perivascular macrophages (pvMΦs), fibroblast-like or mesenchymal cells, endothelial cells, pericytes, and smooth muscle cells. Iterative subclustering identified subtypes of cells within each major non-neuronal class that included novel subpopulations – in addition to resolving different subtypes of endothelial cells (Vanlandewijck et al., 2018) and developmental stages of oligodendrocytes (Marques et al., 2016), we found multiple subtypes or states of astrocytes, oligodendrocytes, and ependymal cells. Ependymal cells shared expression of the histamine synthesis gene *Hdc*, but were further divided into distinct subtypes that differed in expression of cell adhesion and matrix-associated genes as well as signaling peptides such as *Pdyn* (Fig. S2A). *In situ* hybridization (*ISH*) analyses of these differentially expressed genes revealed that these ependymal cell subtypes are topographically organized along major anatomical axes – *Pdyn*-expressing ependymal cells are restricted to ventromedial ventricular walls of the midbrain and hindbrain but are absent from the lateral and third ventricles in the forebrain (Fig. S2B), suggesting zonation of functionally specialized ependymal cell subtypes throughout the ventricular system. Furthermore, the presence of these molecules used for both paracrine and synaptic communication suggests a locally specialized function of ependymal cells in signaling directly to neurons and other cells that express the appropriate G-protein coupled receptors, such as K-opioid and histamine receptors.

141
 142 Neurons ($n = 2,041$ cells), identified by expression of genes required for chemical synaptic
 143 transmission such as *Snap25*, clustered into 5 main classes that could be distinguished by
 144 their neurotransmitter usage. The 5 major neuronal classes (in decreasing order of
 145 abundance) are 5-HT, dopaminergic (DA), GABAergic, glutamatergic, and peptidergic
 146 neurons. Peptidergic neurons were depleted of genes for the synthesis and release of small
 147 molecule neurotransmitters (e.g. *Slc6a4*, *Slc6a3*, *Slc32a1*, *Slc17a6*), but were highly enriched
 148 for the genes encoding neuropeptides such as *Cck*, *Cartpt*, *Ucn*, and *Postn*. Inspection of *ISHs*
 149 from the Allen Brain Atlas (Lein et al., 2007) indicated that these neurons were located in the
 150 Edinger-Westphal nucleus, which is adjacent to the DRN, confirming that our dissection region
 151 spanned most of the DRN along the anterior-posterior axis. Inspection of rhombomere-specific
 152 marker gene expression in the 5-HT neuron cluster showed a lack of markers for R2 (*Hoxa2*)
 153 and R3/5 (*Egr2*) derived neurons in contrast to the expression of R1 markers (*En1* and *En2*),
 154 indicating that our dissection, as intended, excluded most of the median raphe nucleus (Okaty
 155 et al., 2015).

156

157 **Serotonin receptor expression in neuronal and non-neuronal cell types**

158 Analysis of single cell transcriptomic data allowed us to infer signaling between cell types
 159 based on expression of receptors and known ligands. As 5-HT can be released
 160 somatodendritically and from 5-HT axon terminals in the DRN (Colgan et al., 2012; de Kock et
 161 al., 2006; Kaushalya et al., 2008), we examined the expression patterns of 5-HT receptors in
 162 the dataset to infer local 5-HT signaling. Transcripts encoding 8 of the 15 5-HT receptors in the
 163 mouse genome were detected in our dataset (Fig. 2A). Of these *Htr1a*, *Htr1b*, *Htr2c*, *Htr5b*,

and *Htr7* were strongly expressed in different subsets of cells. The autoinhibitory G_i-coupled receptor *Htr1a* was expressed primarily in 5-HT neurons, whereas the G_q-coupled *Htr2c* receptor was expressed in both GABAergic and glutamatergic neurons (Fig. 2B). Additionally, we unexpectedly observed expression of the G_i-coupled *Htr1b* receptor in both 5-HT neurons and pvMΦs of the DRN (Fig. 2C). Examination of *Htr1b* expression in cortex, striatum, and ventral midbrain suggests that expression of this receptor in pvMΦs is unique to the DRN and its close surroundings (Hrvatin et al., 2018; Saunders et al., 2018; Zeisel et al., 2018). Additionally, the absence of abundant neuronal marker genes (e.g. *Snap25*) in pvMΦs indicates that the presence of *Htr1b* transcripts was unlikely to be a result of engulfment of neuronal debris containing mRNA (Fig. 2D). *Htr5b*, which is a pseudogene in humans (Grailhe et al., 2001), was found in ependymal cells and a subset of 5-HT neurons. The G_s-coupled *Htr7* receptor was also found in a small subset of GABAergic and glutamatergic neurons.

Molecularly distinct neuronal subtypes in the DRN

To further resolve the neuronal clusters into separate cell types or subtypes, we analyzed the neuronal clusters separately from the full dataset (see Methods). Subclustering conservatively separated the 2,041 neurons into 18 distinct clusters, which we aggregated into 5 major groups based on similarities in their expression of genes, most notably those involved in the synthesis and release of different neurotransmitters (Fig. 3A). These groups corresponded to the 5 major neuronal classes that were identified from clustering the full dataset, suggesting that neurotransmitter usage is a primary attribute for neuronal cell type identification. However, we also noted significant overlaps in the expression of genes whose loci are typically exploited for the generation of cell type-specific driver lines (Fig. 3B). These genes included *Gad1* and

Gad2, which encode GABA synthetic enzymes and are expressed in GABAergic neurons and a subset of both 5-HT and glutamatergic DRN neurons, as well as *Slc17a6*, which encodes a vesicular glutamate transporter and is expressed in most DRN glutamatergic and DA neurons. These overlaps in expression of “canonical” marker genes are consistent with the release of multiple neurotransmitters by individual neurons, especially by monoaminergic neurons (Granger et al., 2017).

All of the major neuronal cell classes, with the exception of the peptidergic neurons, were comprised of several subclusters that each represent a distinct neuron subtype (Fig. 3B); we found 5 5-HT neuron subtypes, 3 DA neuron subtypes, 5 glutamatergic neuron subtypes, 3 GABAergic neuron subtypes, and 1 cluster co-expressing markers for both GABAergic and glutamatergic neurotransmission (GABA/Glu cluster). To validate the existence of these mixed GABAergic/glutamatergic neurons, we performed multiplexed fluorescent *in situ* hybridization (FISH) for *Slc32a1* and *Slc17a6* as well as *Crhbp*, which was predicted to be strongly expressed by this cluster (Fig. 3C). Cells co-expressing the 3 markers were found within the caudal-linear nucleus (CLi) and dorsal regions of the anterior DRN. Thus, this cluster, representing just 0.08% (32 of 39,411) of cells in the scRNA-seq dataset, corresponds to a bona fide and previously unrecognized neuronal cell type within the DRN that may be a caudal extension of the recently described GABA/Glu neuron group of the ventral midbrain (Root et al., 2018).

GABAergic and glutamatergic neurons shared the most similarities despite differences in neurotransmitter usage. We found that many subtypes of both GABAergic and glutamatergic

neurons shared expression of genes that are enriched in the ventrolateral periaqueductal gray such as *Penk*, as well as the *Htr2c* receptor as described earlier. Within each major group, GABAergic and glutamatergic subtypes differed in their expression of a wide variety of genes that included those for many transcription factors, such as *Nkx2.2*, *Vsx2*, and *Satb1*, as well as peptides and transporters. Additionally, we found a glutamatergic neuron subtype that expressed the vesicular glutamate transporter *Slc17a8* (VGluT3), in contrast to all other DRN glutamatergic neuron subtypes that expressed *Slc17a6* (VGluT2). Consistent with previous descriptions, the *Slc17a8*-expressing glutamatergic subtype also expressed low levels of the transcription factor *Fev* (also known as *Pet1*) similar to 5-HT neurons, despite lacking genes required for the synthesis and release of 5-HT such as *Slc6a4* and *Tph2* (Haugas et al., 2016; Hioki et al., 2010).

Monoaminergic neurons were well separated into distinct DA and 5-HT classes. Although *Vip* was found in all 3 DA neuron subtypes, as previously reported for DRN and CLi DA neurons (Poulin et al., 2018; Poulin et al., 2014), *Vip* expression varied between the 3 subtypes. The *Vip*^{low} DA-I subtype showed more similarities in gene expression with the GABA/Glu neurons of CLi as compared to the *Vip*^{high} DA-III subtype, indicating a corresponding topographical organization of these DA neuron subtypes along the anterior-posterior axis from the CLi to DRN. *Vip*^{low} DA-I subtype neurons also expressed nicotinic receptors including *Chrna4* and *Chrn3* that are also found in GABA/Glu neurons, suggesting differences in nicotinic cholinergic activation of these DA neuron subtypes along the anterior-posterior axis and between DA neurons in CLi versus DRN. The DRN DA neurons lacking expression of nicotinic receptors separated into 2 subtypes, DA-II and DA-III, that differed in expression of genes

related to neurotransmission including peptides, such as *Npw*, and the vesicular glutamate transporter *Slc17a6*, suggesting that DRN DA neurons are functionally heterogeneous.

Genes differentially expressed between DRN 5-HT neuron subtypes

DRN 5-HT neurons separated into 5 distinct subtypes. We constructed a cluster dendrogram using the averaged cluster gene expression to examine the molecular differences between these subtypes (Fig. 4A). We found 333 differentially expressed genes (DE genes) by performing differential expression tests at each node on the cluster dendrogram at a 5% false discovery rate (Benjamini-Hochberg correction). Enrichment tests for gene ontology (GO) terms and analysis of DE genes with annotated functions showed that genes involved in neuronal development and identity specification, such as transcription factors, and genes involved in specifying neuronal connectivity, such as cell adhesion and axon guidance molecules, were overrepresented in the transcripts differentiating the 5-HT subtypes (Fig. S3). A large proportion of DE genes encoded for membrane proteins (GO:0016020 – membrane, 193 of 333 DE genes) with functions in neurotransmission and regulating intrinsic cellular excitability, such as neurotransmitter receptors, ion channels, vesicular transporters, neuropeptides, and other proteins involved in the synthesis or reuptake of neurotransmitters (Fig. 4A).

The cluster dendrogram for 5-HT neuron subtypes showed that the smallest subtype 5-HT-V was the most transcriptionally distinct, and was marked by expression of genes such as *Met*, *P2ry1*, and *Trpc3*, as well as the lack of markers for GABA co-transmission. Inspection of *ISHs*

probing these genes suggests that 5-HT-V subtype neurons are located in the posterior B6 tail of the DRN (Fig. 4B).

The remaining 4 subtypes separated into 2 groups: the first was comprised of subtypes 5-HT-I and 5-HT-II that had enriched expression of genes for GABAergic neurotransmission such as *Gad1* and *Slc6a1*, and the calcium-independent protein kinase *Prkcg*. In contrast to the first subtype group 5-HT-I/II, the second, containing subtypes 5-HT-III and 5-HT-IV, had reduced expression of genes GABAergic neurotransmission such as *Slc6a1*, and expressed genes for glutamatergic transmission. In particular subtype 5-HT-IV expressed high levels of the vesicular glutamate transporter *Slc17a8*. The 5-HT-III/IV group also expressed different cell adhesion and axon guidance molecules from the 5-HT-I/II group, suggesting differences in both cell location and axonal projections between them.

Within the 5-HT-III/IV group, several genes that were enriched in 5-HT-III over 5-HT-IV, such as *Pax5*, *Nxph4*, *Hrh3*, and *Gad1*, were also expressed in subtypes 5-HT-I or 5-HT-II, suggesting that there are features shared between subtypes I, II and III that distinguish subtype III from IV, such as gene expression organized along orthogonal anatomical axes. *ISHs* for genes enriched in these 4 subtypes revealed expression patterns that were consistent with this hypothesis, with the two groups 5-HT-I/II and 5-HT-III/IV largely separated along the medial-lateral axis and subtype IV being separated from the other 3 subtypes along the dorsal-ventral axis. Genes enriched in subtypes 5-HT-I and 5-HT-II were expressed in lateral parts of the DRN (Fig. 4C-D), whereas genes enriched in subtypes 5-HT-III and 5-HT-IV showed enrichment in medial parts of the DRN along the midline (Fig. 4E-F). Additionally, the genes

that were differentially expressed between subtypes 5-HT-III and 5-HT-IV showed graded expression along the dorsal-ventral axis along the midline.

Spatial distribution of 5-HT neuron subtypes in the DRN

Anatomical features are lost during the dissociation of tissue for droplet-based scRNA-seq techniques. *ISH* against a small set of marker genes expressed exclusively in one cell type (see above) can be used to localize the putative location of cell types in complex tissue. However, this approach ignores the full information contained in the many dozens or hundreds of genes whose expression differs in a graded manner across different cellular subtypes. In order to exploit information from many genes differentially expressed across 5-HT neuron subtypes to infer the spatial distribution of transcriptionally defined subtypes, we utilized large imaging datasets from the Allen Brain Atlas, which contain the brain-wide spatial expression profiles of nearly every gene. We built a matrix of spatially binned gene expression for DE genes using images of coronal *ISH* spanning the DRN registered to the Allen Brain Atlas Common Coordinate Framework (see Methods and Fig. S4A). We first used the spatial distribution of *Tph2* expression to define spatial bins (voxels) within the Common Coordinate Framework that contained DRN 5-HT neurons. Subsequently, correlation coefficients between the normalized expression scores for 112 DE genes for each of these voxels and each 5-HT neuron subtype cluster were calculated (Fig. S5C-D). Collections of voxels with high positive correlation coefficients represented the inferred spatial distribution of each subtype within the DRN (Fig. 5). Missing data in the Allen Brain Atlas dataset as well as artifacts apparently introduced in tissue processing that hampered automated *ISH* alignment to the Common Coordinate Framework prevented us from analyzing the full 333 DE genes.

301

302 Correlation maps showed that the 5-HT neuron subtypes identified from the scRNA-seq

303 dataset have distinct but overlapping spatial distributions spread along all three major

304 anatomical axes. Most subtypes were not confined to a specific DRN subregion, with the

305 exception of subtype 5-HT-V (Fig. 5, purple) that showed a tight distribution within the

306 dorsomedial posterior B6 tail of the DRN. The remaining four 5-HT neuron subtypes were

307 found within the larger anterior B7 part of the DRN, and were segregated along both the

308 medial-lateral axis and the dorsal-ventral axis. Subtypes 5-HT-I and 5-HT-II showed the

309 greatest similarities in spatial distribution – both subtypes occupied the dorsolateral subregions

310 in the posterior half of the DRN where they are likely spatially intermingled, consistent with

311 their higher expression of GABAergic transmission genes *Gad1* and *Gad2*. In the more

312 anterior DRN where the lateral wings are absent, subtypes 5-HT-I (Fig. 5, red) and 5-HT-II

313 (Fig. 5, orange) were also be found within the dorsomedial subregion. This overlaps with the

314 distribution of the *Pdyn*-expressing subtype 5-HT-III (Fig. 5, green), which showed the highest

315 correlations with voxels in the dorsomedial part of the DRN in its anterior half. Both subtypes 5-

316 HT-III and 5-HT-IV (Fig. 5, blue) showed higher correlations with voxels along the midline, but

317 were separated along the dorsal-ventral axis with the *Slc17a8*-enriched 5-HT-IV subtype

318 occupying most of the ventral DRN. Subtype 5-HT-IV was also most evenly distributed along

319 the anterior-posterior axis compared to the other subtypes.

320

321

5-HT neuron subtype distributions coincide with different projection-defined subpopulations

The nuclei of the basal ganglia are major targets of DRN 5-HT neurons, with approximately one-third of all DRN 5-HT neurons innervating the striatum (Str) (Steinbusch et al., 1981). In addition to the extensive anatomical connectivity between the basal ganglia and DRN, both structures have motor and cognitive functions, and have been implicated in disorders that affect motor control and motivation such as impulsivity, obsessive-compulsive disorder, and major depressive disorder (Di Matteo et al., 2008; Miguez et al., 2014; Pauls et al., 2014; Schilman et al., 2010). Although the DRN has many shared functions with the basal ganglia, DRN neurons are also involved in modulation of sensory pathways, limbic and neuroendocrine systems, and brainstem motor nuclei, and it has been proposed that anatomically segregated subsets of DRN 5-HT neurons form separate efferent pathways to perform these different functions (Hale and Lowry, 2011; Lowry, 2002; Muzerelle et al., 2016; Waselus et al., 2011). Therefore to compare the distribution of the 5-HT neuron subtypes from our scRNA-seq dataset with those of projection-defined neuron subpopulations in the DRN, we performed retrograde tracing from several nuclei of the basal ganglia, structures connected to basal ganglia circuits such as frontal and prefrontal cortical regions, as well as more functionally and anatomically distant structures that include thalamic sensory nuclei, such as the dorsal lateral geniculate nucleus (dLGN).

To map the distribution of projection-defined DRN neuron subpopulations, we performed retrograde tracing using glycoprotein-deleted rabies viruses (RbV) injected into brain regions known to receive inputs from DRN 5-HT neurons (Fig. 6A). Cells infected via their axons by

RbV were fluorescent, and their positions were manually registered onto an averaged Nissl coronal template from the Allen Brain Atlas (Fig. 6B-C). Cells were counted in 50 x 50 μm bins, and bin counts were normalized by the total cell count to obtain the probability distributions for each projection-defined subpopulation. Probability distributions are displayed as heatmaps overlaid on reference template images to compare their distributions.

Most projection-defined subpopulations were located either ipsilateral to the injection site or along the midline, with the exception of the habenula-projecting neurons which were found in both ipsilateral and contralateral lateral wings of the DRN (Fig. S6). Within the cortical-projecting group, frontal- and prefrontal-projecting subpopulations were differentially distributed along the anterior-posterior axis of the DRN – M1-projecting neurons were relatively confined to the anterior half of the DRN, whereas mPFC-projecting neurons were found in both anterior and posterior halves. Consistent with previous reports (Ren et al., 2018; Waterhouse et al., 1986), we found that most subcortical-projecting neurons were located in the dorsal DRN, whereas most cortical-projecting neurons were located in the ventral DRN. Although there was a crude separation of cortical- and subcortical-projecting subpopulations along the dorsal-ventral axis, there were considerable overlaps between their distributions, preventing the delineation of a clear boundary between cortical- and subcortical-projecting groups. The Str-projecting and M1-projecting subpopulations were largely segregated into the dorsal and ventral DRN respectively. However, there were overlaps in their distributions at intermediate levels – both Str-projecting and M1-projecting neurons were found in the ventrolateral DRN (outlined in cyan in Fig. 6D column 3) and dorsal border of the ventromedial DRN. Double

retrograde tracing experiments also showed that DRN neurons innervating both Str and M1 were often found in these regions (Fig. S7).

Projection-defined subpopulations that innervated different subcortical targets, such as the Str-projecting versus dLGN-projecting subpopulations, were spatially segregated within the DRN (Fig. 6D). dLGN-projecting neurons were mostly located in dorsolateral subregions at more posterior levels, whereas Str-projecting neurons were mostly in the dorsomedial subregion at more anterior levels. The distributions of subpopulations innervating related structures within the basal ganglia were more similar (Fig. 6E) and, while the subpopulations innervating the external globus pallidus (GPe) and Str were most similar, the subpopulations innervating the Str and nucleus accumbens (NAc, also called the ventral striatum) showed a larger difference. This difference was largely driven by the presence of NAc-projecting neurons in posterior parts of the DRN where mPFC-projecting neurons were also located, whereas Str-projecting DRN neurons were relatively confined to the anterior half of the DRN (Fig. S8). This is also consistent with differences in the function of Str and NAc and their relation to functional differences between the anterior and posterior DRN (Lowry, 2002; Van Bockstaele et al., 1993).

Differential expression of many axon guidance and cell adhesion molecules between 5-HT neuron subtypes predicts that 5-HT subtypes innervate different brain regions. Two models for how these molecularly-defined subtypes relate to projection-defined subpopulations that would be consistent with this hypothesis are (i) 5-HT neuron subtypes have non-overlapping axonal projection fields and thus a projection-defined subpopulation is comprised of a single subtype

and is contained within the subtype's distribution, or (ii) different 5-HT neuron subtypes can innervate the same structure and thus projection-defined subpopulations can be comprised of one or more subtypes. To predict the 5-HT neuron subtypes present in different projection-defined neuron subpopulations, we compared the distributions of projection-defined subpopulations with the inferred 5-HT neuron subtype distributions.

It has been reported that cortical-projecting subpopulations of DRN 5-HT neurons express *Slc17a8*, in agreement with the extensive overlap between the spatial distribution of cortical-projecting neurons and *Slc17a8* expression (Ren et al., 2018). This suggests that cortical-projecting subpopulations should correspond to subtype 5-HT-IV from the scRNA-seq dataset, which is *Slc17a8*-expressing and distributed to the ventral DRN. Additionally, we would predict that the Str-projecting subpopulation corresponds to the subtype 5-HT-III, since their distributions overlap extensively in the dorsomedial DRN. Consistent with our hypothesis that 5-HT neuron subtypes innervate different brain regions, we found that the inferred distributions of each 5-HT neuron subtype coincides with a different set of projection-defined subpopulations – the distribution of subtype 5-HT-III was most similar to the distribution of Str-projecting neurons (Fig. 6F), whereas the distribution of subtype 5-HT-IV was more similar to that of M1-projecting neurons (Fig. 6G). However, neither Str-projecting nor M1-projecting subpopulations were contained within the distribution of a single 5-HT neuron subtype. Str-projecting neurons in the ventrolateral DRN (marked cyan in Fig. 6D, 6F, and 6G), where neurons innervating both Str and M1 are located, fell within the distribution of subtype 5-HT-IV but not of subtype 5-HT-III. This suggests that Str is a target of multiple molecular subtypes of

5-HT neurons, and supports the model that some structures are innervated by multiple 5-HT neuron subtypes due to overlaps in the axonal projection fields of different subtypes.

Striatal-projecting 5-HT neurons are transcriptionally heterogeneous

To determine the molecular identities of individual projection-defined DRN neurons, we combined RbV-mediated retrograde tracing with multiplexed FISH for markers of 5-HT neuron subtypes. We focused on determining the subtype identity of Str-projecting 5-HT neurons, since their location overlaps with the distributions of multiple 5-HT neuron subtypes. Neurons projecting to Str were labeled using axon-infecting unpseudotyped SADΔG B19 rabies viruses (B19G-SADΔG-tdTomato) injected into the ventrolateral Str. Rabies-infected neurons were identified by expression of the viral transcript *B19N* using smFISH (RNAscope probe: RABV-gp1), and 5-HT neurons were identified based on expression of the serotonin reuptake transporter gene *Slc6a4* (Fig. S9). The subtype identity of RbV-infected 5-HT neurons was identified by expression of genes that were highly enriched in each subtype: *Trh* for subtype 5-HT-I, *Pdyn* for subtype 5-HT-III, *Cbln2* and *Slc17a8* for subtype 5-HT-IV. *ISH* for each of these subtype markers was performed on separate sets of RbV-labeled cells (Fig. 7).

We found that Str-projecting DRN 5-HT neurons expressed the subtype 5-HT-III marker *Pdyn* (52%, 39 of 75 RbV-labeled 5-HT neurons) or the 5-HT-IV marker *Cbln2* (46%, 49 of 106 RbV-labeled 5-HT neurons), consistent with the overlap in the distribution of this projection-defined subpopulation with the inferred distributions of these two distinct subtypes. A subset of Str-projecting neurons also expressed *Slc17a8* (57%, 70 of 123 RbV-labeled 5-HT neurons), which is enriched in 5-HT-IV but also expressed in 5-HT-III at lower levels. Few Str-projecting

neurons expressed *Trh* (4%, 4 of 102 RbV-labeled 5-HT neurons). This low proportion of *Trh*-expressing neurons is consistent with the low occurrence of *Trh* expression in subtypes 5-HT-III and 5-HT-IV, and suggests that Str-projecting 5-HT neurons are unlikely to be subtype 5-HT-I neurons. Therefore, our results support the hypothesis that the Str-projecting DRN 5-HT neuron subpopulation is molecularly heterogeneous, and is comprised of at least two transcriptionally distinct 5-HT neuron subtypes.

Innervation of basal ganglia by a *Pdyn*-expressing 5-HT neuron subtype

The distribution of 5-HT-III subtype neurons overlapped with that of several projection-defined subpopulations that innervated nuclei of the basal ganglia beyond Str. To validate that the 5-HT-III subtype innervates the basal ganglia, we used an intersectional genetic targeting strategy to perform anterograde tracing from this subtype based on its enriched expression of *Pdyn*. We generated *Pet1-Flpe;Pdyn-IRES-Cre;LSL-FSF-ReaChR:mCitrine* mice in which *Pdyn*⁺;*Pet1*⁺ co-expressing neurons and their processes are fluorescently labeled by mCitrine-tagged ReaChR. To compare the innervation patterns of this subtype with that of the full DRN 5-HT neuron population, we also performed anterograde tracing from DRN *Pet1*⁺ neurons by injecting Cre-dependent adeno-associated viruses into the DRN of *Pet1-Cre* mice, labeling *Pet1*⁺ neurons in the dorsal and ventral DRN with EGFP and tdTomato respectively (Fig. 8A). mCitrine-labeled axons from *Pdyn*⁺;*Pet1*⁺ neurons were found in a subset of regions innervated by DRN *Pet1*⁺ neurons (Fig. 8B-F, Fig. S10). Of the regions innervated by both DRN *Pet1*⁺ neurons and *Pdyn*⁺;*Pet1*⁺ neurons, the output nuclei of the basal ganglia, including the ventral pallidum (VP), entopeduncular nucleus (EP), and substantia nigra pars reticulata (SNr), were most densely innervated by *Pdyn*⁺;*Pet1*⁺ neurons (Fig. 8B-D). In contrast, sensory

structures, such as the dLGN (Fig. 8E), and limbic structures, such as the hypothalamus (Fig. 8F) were not innervated by *Pdyn*⁺; *Pet1*⁺ neurons, despite receiving dense input from DRN *Pet1*⁺ neurons. These results therefore demonstrate that the *Pdyn*⁺ subtype 5-HT-III neurons broadly but selectively innervate structures that are either a part of or functionally linked to the basal ganglia, and are unlikely to be involved in sensory modulation.

DISCUSSION

Here we present a transcriptomic map of cell types in and around the DRN, and outline the spatial organization of these cell types based on information contained in their molecular profiles. By overlaying transcriptional and anatomical features onto a common reference atlas, we describe the molecular basis for the organization of DRN 5-HT neurons into distinct subsystems. We uncovered 5 subtypes of DRN 5-HT neurons based on their gene expression profiles and showed that these are organized into distinct spatial domains within the DRN that are segregated along all three major anatomical axes. However, the spatial organization of molecularly defined 5-HT neurons does not conform to anatomical subdivisions as defined by cytoarchitecture of the DRN or the projection targets of 5-HT axons. The overlapping spatial distributions of 5-HT subtypes demonstrate the need for precise molecular and genetic approaches to dissect the function of each subtype. We also define a *Pdyn*-expressing 5-HT neuron subtype that is well positioned to broadly but specifically alter the input and output of basal ganglia circuits, potentially mediating the modulation of motor control, decision making, and reinforcement learning by internal state.

Anatomical organization of DRN 5-HT neuron subtypes

We present a physical map combining both transcriptional and anatomical features and show that molecularly distinct DRN 5-HT neuron subtypes are spatially segregated into distinct anatomical subdomains and innervate different but overlapping targets. We reconstructed the spatial distribution of each 5-HT subtype using spatial correlation analysis of gene differentially expressed between subtypes and showed that each cytoarchitecturally-defined DRN subregion contains different molecularly-defined 5-HT subtypes. The subregional distribution of

5-HT subtypes relates well to past studies reporting subregion-specific anatomical and molecular differences that are consistent with our integrative map of 5-HT subtype features.

Of the 5 subtypes, the 5-HT-V was the most transcriptionally distinct and spatially restricted, and was found in a tight dorsomedial cluster in the posterior B6 tail of the DRN. Previous reports have suggested that the B6 5-HT neuron cluster is transcriptionally more similar to 5-HT neurons in the median raphe nucleus, despite being a part of the cytoarchitecturally-defined DRN (Commons, 2015). This has led to the proposal that the posterior DRN is an extension of the median raphe nucleus (MRN), although this remains to be validated using single cell transcriptomic profiling of both DRN and MRN 5-HT neurons. At the molecular level, 5-HT-V subtype neurons express a distinct set of receptors compared to the other 4 DRN 5-HT neuron subtypes. The localization of this subtype to the dorsomedial posterior B6 tail of the DRN also suggests that this subtype may innervate ventricular and subventricular regions and the choroid plexus and primarily target non-neuronal cells (Muzerelle et al., 2016). The transcriptomic profile of this subtype we present here will aid in the development of molecular and genetic approaches for targeting this subtype, and may facilitate studies on serotonergic modulation of adult neurogenesis in the subventricular zone, as well as production and regulation of cerebrospinal fluid (CSF) by cells in the choroid plexus and ependymal lining of the ventricles (Banasr et al., 2004; Fisone et al., 1995; Moskowitz et al., 1979; Young et al., 2011).

The ventral DRN, comprised of the ventromedial subregion (or DRV) and interfascicular subregion (or DRI), contains mostly *Slc17a8*-enriched 5-HT-IV subtype neurons that innervate

cortex. We noted that 5-HT-IV neurons were distributed throughout most of the anterior-posterior extent of the ventral DRN, although it is suggested that there is a topographical organization of cortical projecting 5-HT neurons along this axis. We speculate that this may reflect the broad and divergent cortical projections of individual 5-HT-IV neurons that collectively span most of the cerebral cortex. Alternatively, additional heterogeneity within the 5-HT-IV subtype may explain variation along the anterior-posterior axis that may be revealed with deeper sequencing.

In comparison, the dorsolateral DRN, also called the lateral wings of the DRN (lwDRN) and ventrolateral DRN (DRVl), showed strongly negative correlations with the 5-HT-IV subtype, particularly in the posterior half of the DRN where there is clearer spatial separation of *Tph2*⁺ neurons into medial and lateral compartments. Subtypes 5-HT-I and 5-HT-II were intermingled in this region, which is enriched in *Trh*, a 5-HT-I marker. The dorsolateral subregion innervates many subcortical sensory and hypothalamic nuclei, in addition to motor nuclei in the brainstem (Lee et al., 2008; Muzerelle et al., 2016). We speculate that 5-HT-I and 5-HT-II form the cellular bases for the separation of DRN 5-HT projections to brainstem motor regions versus sensory/limbic regions respectively, given the expression of the TRH receptor gene (*Trhr*) in several brainstem motor nuclei innervated by the DRN, such as the facial motor nucleus (Allen Brain Atlas). Further experiments using retrograde tracing and molecular profiling of DRN 5-HT neurons innervating these structures can be performed to evaluate these hypotheses. Additionally, the close spatial proximity of these 2 subtypes also presents a plausible mechanism for competitive inhibition between these separate subsystems via 5-HT_{1A}

receptors and local 5-HT release, which may be relevant to selective sensory modulation by movement or changes in behavioral state (Hall et al., 2010; Yokogawa et al., 2012).

Although we show that 5-HT subtypes have distinct spatial locations, we also found considerable overlaps in their distributions, particularly within the dorsomedial subregion in the anterior DRN that contains many basal ganglia-projecting 5-HT neurons. While the *Pdyn*-expressing 5-HT-III subtype was localized to the dorsomedial subregion, subtypes 5-HT-I and 5-HT-II were also found in this subregion in the anterior third of the DRN despite being distributed to dorsolateral subregions in more posterior sections. Furthermore, a detailed comparison of the 5-HT subtype distributions with cytoarchitecturally-defined subregion boundaries showed that subtype distributions are not confined within these subregion boundaries, especially in the anterior half of the DRN. The poor correspondence between molecularly-inferred and cytoarchitecturally-defined spatial domains cautions against the use of anatomical subregions for targeting 5-HT subsystems.

Molecular organization of DRN 5-HT subsystems

5-HT neurons are organized into discrete subsystems that (i) have distinct and dissociable behavioral functions, and (ii) are comprised of 5-HT neurons possessing unique molecular, physiological, and anatomical properties. However, the complex architecture of the DRN has impeded efforts to understand the interrelationship of these three aspects of 5-HT diversity, as necessary to study the differential properties and functions of each subsystem and its distinct subtype of 5-HT neuron. Given the extensive overlaps in the distribution of different 5-HT neuron subsets at the anatomical level, we were motivated by the hypothesis that a

transcriptome-based molecular definition of 5-HT neuron subtypes was required to both understand the organization of heterogeneous 5-HT neuron subtypes as well as to enable their precise targeting for functionally analyses. Consistent with this hypothesis, our results suggest that many of the physiological and anatomical differences between 5-HT neuron subtypes are a result of molecular differences specified by expression of overlapping but distinct transcriptional networks. Furthermore, we find differential expression of transcription factors across subtypes that may underlie many of these molecular differences that are specified during the development of each subtype. It is likely that further differences and subtypes may be resolved with deeper sequencing of single cells, and at multiple time points along the developmental trajectory of 5-HT neurons. Eventually these molecular approaches will be well complemented by whole-brain reconstructions of axons of single neurons (Economo et al., 2016; Gong et al., 2016) as well as spatial transcriptomics (Chen et al., 2015; Wang et al., 2018).

Local interactions between DRN cell types

Our scRNA-seq dataset yields predictions about local interactions involving DRN cells, including with non-neuronal cells, based the expression patterns of known receptor-ligand pairs. For example, the expression of *Hdc* in ependymal cells suggests that ependymal cells may signal to nearby neurons via non-synaptic release of histamine. Histaminergic paracrine signaling from ependymal cells can exert differential effects on various neuronal subtypes based on proximity to the cerebral aqueduct and differential expression of histaminergic receptors. Notably, the histamine receptors *Hrh1* and *Hrh3* are expressed in 5-HT subtypes 5-HT-I, 5-HT-II, and 5-HT-III, which are all located in dorsal DRN subregions in close proximity to

the cerebral aqueduct. In contrast, 5-HT-IV subtype neurons, which are in ventral subregions further from the aqueduct, do not express detectable levels of histamine receptors. Enrichment of the G_i -coupled *Hrh3* receptor in 5-HT-III further suggests that histamine may inhibit this subtype while increasing the excitability of 5-HT-I and 5-HT-II neurons. Release of peptides such as *Pdyn* from a subset of ependymal cells can also have differential effects dependent on the expression pattern of the K-opioid receptor. Additionally, ependymal cells may communicate via secretion of these transmitters and peptides into the CSF. Transmitters and peptides released into the ventricular system can have long range effects facilitated by the flow of CSF and signal to neuronal cells extending processes to the ventricular walls, including some 5-HT neurons, as well as non-neuronal cells including ventricular immune cells and choroid plexus cells.

We also found that pvMΦs within or in close proximity to the DRN express the G_i -coupled *Htr1b* receptor, unlike pvMΦs in brain regions that do not contain 5-HT neurons. This suggests that pvMΦs in different brain regions may be specialized via differential expression of neurotransmitter receptors to be specifically tuned to monitor their local environment and respond to changes in neuronal activity. Activation of G_i -coupled pathways on pvMΦs via 5-HT_{1B} receptors is also a potential mechanism for the regulation of macrophage polarization and inflammatory responses by tonic 5-HT release within the DRN, which may be relevant to the increasing importance of neuroinflammatory pathways in the etiology of psychiatric disorders (Brisch et al., 2017; Howerton et al., 2014; Watkins et al., 2014).

601 The diversity of neuronal subtypes in and around the DRN also highlights the importance of
602 elucidating local circuitry with knowledge of the molecular identity of both pre- and post-
603 synaptic neurons. For direct signaling between 5-HT neurons, somatodendritic release of 5-HT
604 and activation of inhibitory 5-HT_{1A} receptors on adjacent 5-HT neurons is likely to mediate
605 lateral inhibition between the 5-HT neurons of the same subtype, due to the spatial clustering
606 of the subtypes. However, GABAergic and/or glutamatergic neurons may be excited by
607 adjacent 5-HT neurons via activation of their 5-HT_{2C} and 5-HT₇ receptors to mediate indirect
608 interactions between 5-HT neuron subtypes. These interactions may be either synergistic if
609 mediated by glutamatergic neurons innervating other 5-HT subtypes, or antagonistic in a form
610 of lateral inhibition via GABAergic interneurons. Subtype-specific connections between 5-HT
611 neurons and local GABAergic and glutamatergic neurons can mediate interactions between
612 different subsystems and may contribute to the contrasting and opposing functions ascribed to
613 the DRN as a whole. Although 5-HT neurons have been reported to form local connections
614 (Weissbourd et al., 2014), it is currently unknown how the 18 neuronal subtypes we have
615 described are organized into local circuits. To generate models of these local circuits, the
616 connectivity between DRN and ventrolateral PAG neurons will need to be mapped with
617 subtype-level molecular resolution. This will likely require the use of retrograde tracing
618 techniques with improved specificity for targeting neuronal subtypes in combination with spatial
619 transcriptomic methods that are compatible with the large volume of the DRN. These methods
620 can also be extended to examine the interactions between larger networks of 5-HT
621 subsystems distributed across the raphe nuclei, which have been shown to be interconnected
622 based on conditional anterograde tracing using intersectional targeting of 5-HT neurons
623 originating from different embryonic rhombomeres (Bang et al., 2012).

624

625 **A 5-HT subsystem targeting basal ganglia circuits**

626 The transcriptomic information we obtained on DRN 5-HT neuron subtypes allowed us to
 627 access a specific 5-HT subsystem that innervates circuits of the basal ganglia. We showed
 628 that the subsystem comprised of the *Pdyn*-expressing subtype 5-HT-III sends broad
 629 projections to both input and output nuclei of the basal ganglia, while avoiding other sensory
 630 and limbic structures, which have distinct functions from the basal ganglia and are likely to
 631 receive inputs from other DRN 5-HT neuron subtypes. Although we also showed that the basal
 632 ganglia receives inputs from multiple 5-HT neuron subtypes, particularly in the case of the
 633 striatal-projecting subpopulation, the dense innervation of basal ganglia output nuclei by 5-HT-
 634 III neurons suggests that this 5-HT subsystem has a prominent role in the regulation of motor
 635 output and action selection through its effects on the activity of basal ganglia output nuclei. We
 636 also speculate that 5-HT release from this subsystem may have different effects on distinct
 637 output channels of the basal ganglia, given the differential expression of 5-HT receptors on
 638 distinct subpopulations of SNr and EP projection neurons (Saunders et al., 2018; Wallace et
 639 al., 2017). The targeting of distinct channels or subcircuits within the basal ganglia may also be
 640 consistent with the innervation of the striatum by multiple 5-HT neuron subtypes given the
 641 topographical arrangement of convergent cortical inputs into distinct domains within the
 642 striatum (Hintiryan et al., 2016), since it is plausible that distinct striatal domains are each
 643 innervated by a different but functionally related 5-HT neuron subtype. Subcircuit-specific
 644 effects of 5-HT within the basal ganglia would also have implications on models for the function
 645 of 5-HT in decision-making and motor control (Migueluez et al., 2014; Reed et al., 2013),

although further work is needed to elucidate the structural and functional organization of these subcircuits in the basal ganglia (Calabresi et al., 2014).

Our results provide a resource for the design of intersectional strategies for the functional dissection of DRN cell types. The *LSL-FSF-ReaChR:mCitrine* intersectional reporter line that we used for conditional anterograde tracing will also be suitable for optogenetic perturbation experiments *in vivo* to investigate the circuit and behavioral functions of these distinct 5-HT subsystems. Greater spatial specificity can be achieved through the use of tapered optic fibers for site-specific light delivery (Pisanello et al., 2014), intersectional viral constructs (Fenno et al., 2014) optimized for expression in cell types of interest, and the development of additional Cre and Flp recombinase driver lines with improved specificity to increase the number of subtypes and subsystems that can be accessed through genetic and molecular approaches. The functional studies facilitated by the development of these additional tools will provide further mechanistic insights into the coordinated action of distinct cell types and subsystems of the DRN in the regulation of behavior.

ACKNOWLEDGEMENTS

We thank the Dymecki (HMS) and Lowell (BIDMC) Labs for generously providing transgenic mouse lines; the HMS ICCB Single Cell Core for assistance with scRNA-seq experiments on the InDrop platform; S. Hrvatin and A. Nagy (Greenberg Lab, HMS) for advice and help with scRNA-seq protocols and analysis pipelines; B.K. Lim (UCSD) and I.R. Wickersham (MIT) for advice and reagents for rabies virus production; the Bauer Core Facility at Harvard University for sequencing support; the HMS Neurobiology Imaging Facility for confocal microscopy support (P30 NS072030); and members of the Sabatini Lab for helpful discussions. We also thank our undergraduate students M. Henson, A. Mustoe, and L. Chung for technical assistance, J. Levasseur for genotyping and animal husbandry, and L. Worth for administrative assistance. This work was supported by funding from the Howard Hughes Medical Institute (B.L.S.), National Institutes of Health (R01 MH100568 and R01 NS103226 to B.L.S.), a Harvard Brain Initiative Bipolar Disorder Seed Grant (B.L.S.), a Samsung Scholarship (M.H.), the Lefler Center for the Study of Neurodegenerative Disorders (M.H.), the HMS Department of Neurobiology Graduate Fellowship (K.W.H.), and the HMS Stuart H.Q. & Victoria Quan Fellowship in Neurobiology (K.W.H.).

AUTHORS CONTRIBUTIONS

K.W.H. and B.L.S. designed the experiments, and K.W.H. performed most of the experiments and data analysis. N.E.O. assisted with stereotaxic injections for anatomical tracing, sample preparation for histology, and data analysis for retrograde tracing. A.C.P. assisted with rabies virus production and fluorescent *in situ* hybridization experiments. M.H. assisted with scRNA-seq experiments. J.E.B. and M.C. assisted with imaging data processing and analysis. K.W.H. and B.L.S. wrote the manuscript with contributions from the other authors.

COMPETING INTERESTS

The authors have no competing interests to declare.

FIGURE LEGENDS

Figure 1: High-throughput single cell transcriptomic profiling of the DRN.

(A) Schematic for scRNA-seq using the inDrop platform. (1) Tissue containing the DRN and surrounding regions was microdissected from acute coronal brain slices prepared from adult C57BL/6J mice. (2) Tissue chunks were digested in a cocktail of proteases and inhibitors of neuronal spiking, transcription, and translation. Digestion was followed by trituration and filtration to obtain a cell suspension. (3) Single cells were encapsulated using a droplet-based microfluidic device for cell barcoding and mRNA capture.

(B) t-SNE plot of the processed dataset containing 39,411 cells from 8 animals. Cells are color-coded according to the cluster labels shown in (C).

(C) Left: Dendrogram with cell class labels corresponding to clusters shown in (B). Right: Dot plot displaying expression of example marker genes used to identify each major cell class. The color of each dot (blue to red) indicates the relative expression of each gene whereas the dot size indicates the fraction of cells expressing the gene.

Figure 2: Serotonin receptors are expressed in both neurons and non-neuronal cells.

(A) Dot plots showing expression of the serotonin receptors present in the scRNA-seq dataset in each major cell class. *Htr1a* is expressed specifically in 5-HT neurons, whereas *Htr1b* is expressed in both 5-HT neurons and perivascular macrophages. *Htr2c* is expressed in both GABAergic and glutamatergic neurons. *Htr5b* is expressed in ependymal cells and a subset of 5-HT neurons. *Htr7* is expressed in subsets of GABAergic and glutamatergic neurons. The remaining 5-HT receptors were detected at low levels.

(B) t-SNE plots with the region containing neuronal clusters enlarged to show expression of *Htr1a* (bottom, left) or *Htr2c* (bottom, right) in individual cells. Cells are color-coded by expression of each transcript. Scale bars are in log-normalized UMI-filtered counts for the respective transcripts.

(C) t-SNE plots with cells color-coded by their expression of *Htr1b*. Regions containing neuronal or perivascular macrophage clusters are enlarged.

(D) t-SNE plots with cells color-coded by their expression of the neuron-specific transcript *Snap25*. Regions containing neuronal or perivascular macrophage clusters are enlarged. *Snap25* transcripts are abundant in all neuronal clusters but not in perivascular macrophages, suggesting that *Htr1b* transcripts in perivascular macrophages are unlikely to be a result of engulfment of neuronal debris.

Figure 3: Neuron subtypes can be distinguished transcriptionally.

(A) t-SNE plot of 2,041 neurons. The main neuron types were defined by the expression of genes necessary to make or release specific neurotransmitters or neuropeptides, and are highlighted by the shaded regions. Several subtypes of each class of neuron, designated by the cell color, can be contained in each shaded region. Color codes for subtype identities correspond to column headers in (B). The cluster outlined in red corresponds to cells expressing both glutamatergic and GABAergic markers.

(B) Heatmap showing the relative expression of selected genes that are enriched in each neuron subtype. Marker genes used to identify major neuronal cell types by their neurotransmitters are labeled in red.

(C) Fluorescent *in situ* hybridization validating the existence of cells expressing both GABAergic and glutamergic markers. Cells expressing *Slc32a1*, *Slc17a6*, and *Crhbp* were found in anterior regions of the DRN in the caudal linear nucleus (CLi) and dorsomedial DRN in close proximity to the cerebral aqueduct. The regions indicated by the yellow boxes are shown enlarged on the right.

Figure 4: Characterization of genes differentially expressed between serotonergic neuron subtypes.

(A) Expression heatmaps of selected genes with functional annotation that are differentially expressed between DRN 5-HT neuron subtypes. A total of 333 differentially expressed (DE) genes were found (5% false discovery rate, Benjamini-Hochberg correction). A large proportion of DE genes encode for cell surface and transmembrane proteins. Genes shown are categorized into five groups: transcription factors, cell adhesion and axon guidance molecules, transmembrane receptors, ion channels, and neurotransmission-related genes.

(B-F) *In situ* hybridizations from the Allen Brain Atlas showing the expression patterns of selected DE genes enriched in each of the five 5-HT neuron subtypes. Many DE genes are not expressed uniformly throughout the DRN and are instead spatially heterogeneous along the anterior-posterior, medial-lateral, and dorsal-ventral axes, suggesting that 5-HT neuron subtypes are differentially distributed across spatial domains.

Figure 5: 5-HT neuron subtypes are distributed in distinct but overlapping spatial domains.

Inferred spatial distributions of 5-HT neuron subtypes displayed as a map of correlation coefficients between profiles of gene expression of each subtype and each spatial bin. Each column shows the correlation map for each 5-HT neuron subtype at different coronal sections along the anterior-posterior axis of the DRN (rows). Only bins with positive correlation coefficients greater than 0.1 are shown, and maps were smoothed using a 2D Gaussian filter (1SD) for display. Correlation maps are overlaid on the averaged *Tph2* expression (grayscale, based on *ISH* data from the Allen Brain Atlas). Correlation maps for subtypes I and II suggest that they are largely intermingled in the dorsolateral DRN, with some overlap in the anterior DRN with subtype III in the dorsomedial DRN. Subtype IV was enriched in the ventral regions of the DRN, while subtype V was highly restricted to the posterior B6 tail of the DRN that was highly enriched in expression of the subtype V candidate marker *Met*. Scale bars: 500 μ m.

Figure 6: Projection-defined DRN neuron subpopulations overlap with multiple 5-HT subtypes.

(A) Schematic of retrograde tracing experiments in which unpseudotyped rabies viruses (SAD Δ G B19 stain) was used to infect and label neurons whose axons innervate the virus injected target region (GPe in this example).

(B) Image of a coronal section of the DRN showing rabies-labeled, GPe-projecting neurons. Brains were fixed 7 days post-injection for histology, and 5-HT neurons in the DRN were visualized using immunohistochemistry against TPH2. Sections were counterstained using a fluorescent Nissl stain (Neurotrace).

779 **(C)** The location of all rabies-labeled cells within the DRN and vIPAG, such as the GPe-
780 projecting cells in (B), were manually registered onto a coronal template derived from the
781 averaged Allen Brain Atlas coronal Nissl stain. Labeled neurons outside of this region of
782 interest, such as the PPN and dorsal PAG, were not included.

783 **(D1-5)** Distributions of Str-projecting (green), M1-projecting (blue), and dLGN-projecting (red)
784 subpopulations, displayed as a probability density map (50 μm x 50 μm bins) overlaid on the
785 coronal template. Coronal sections shown are centered in panel D3 at the maximum density of
786 the Str-projecting population. Str- and M1-projecting populations were largely separated along
787 the dorsal-ventral axis, with some overlap. Co-labeled neurons projecting to both Str and M1
788 were typically found in the ventrolateral DRN, outlined in cyan in D3, and the ventromedial
789 DRN.

790 **(E)** Pairwise correlations between the distributions of projection-defined subpopulations.
791 Correlations between the Str-projecting subpopulation were higher with other subpopulations
792 that also innervate nuclei of the basal ganglia, compared with subpopulations innervating
793 functionally distinct targets such as M1 or dLGN.

794 **(F-G)** Overlap between the distributions of neurons innervating Str (F) or M1 (G) and the 5-HT
795 neuron subtype distributions at AP = -4.30 mm. Distributions of each projection-defined
796 subpopulation are represented as probability maps (magenta) overlaid on the averaged *Tph2*
797 expression. Subtype distributions are represented as color-coded outlines corresponding to the
798 colors used in Fig. 4 for each subtype. Str-projecting neurons largely fell into regions occupied
799 by both 5-HT-III and 5-HT-IV subtypes, suggesting molecular heterogeneity within this
800 projection-defined population. M1-projecting neurons were more confined to the ventral DRN,
801 overlapping with the distribution of the 5-HT-IV subtype. Scale bars: 500 μm .

802

803 **Figure 7: Striatum receives inputs from multiple DRN 5-HT neuron subtypes.**

804 Multiplexed fluorescent *ISH* was used to identify rabies-infected Str-projecting 5-HT neurons in
 805 the DRN and quantify their expression of candidate 5-HT neuron subtype markers. Rabies-
 806 infected neurons are identified by expression of the virus transcript *B19N*. Confocal images of
 807 the DRN from representative coronal sections are shown in column 1, and regions marked
 808 yellow in are expanded and separated by channel in columns 2-4. The proportions of DRN 5-
 809 HT neurons that express each candidate subtype marker are summarized in pie charts in
 810 column 5. Approximately half of the Str-projecting 5-HT neurons express the subtype III marker
 811 *Pdyn* (row A), and a similar proportion express subtype IV enriched genes such as *Slc17a8*
 812 (row B) and *Cbln2* (row C). Most Str-projecting 5-HT neurons do not express the subtype I
 813 candidate marker *Trh* (row D).

814

815 **Figure 8: *Pdyn*⁺ 5-HT neurons target basal ganglia circuits.**

816 **(A)** Conditional anterograde tracing from subsets of 5-HT neurons. Anterograde tracing from
 817 *Pet1*⁺ DRN neurons was performed by injecting AAV2/1-CAG-FLEX-EGFP into the dorsal
 818 DRN and AAV2/1-CAG-FLEX-tdTomato into the ventral DRN of *ePet1-Cre* mice. A coronal
 819 section from the DRN injection site containing *Pet1*⁺ cells expressing either EGFP or tdTomato
 820 is shown on the left in (A1). *Pdyn*⁺; *Pet1*⁺ neurons were labeled by intersectional genetic
 821 targeting with a Cre- and Flp-dependent reporter line *R26-LSL-FSF-ReaChR:mCitrine* crossed
 822 to *Pdyn-IRES-Cre;Pet1-Flpe* mice. *Pdyn*⁺; *Pet1*⁺ expressing ReaChR:mCitrine in the DRN are
 823 shown on the right in (A2). 5-HT neurons are labeled by immunostaining for TPH2.

824 **(B – F)** Axonal projections of *Pdyn*⁺*Pet1*⁺ neurons were compared to projections of DRN *Pet1*⁺
825 neurons using separate approaches for conditional anterograde tracing. *Pdyn*⁺*Pet1*⁺ neurons
826 densely innervate many output nuclei of the basal ganglia, including VP (B2), EP (C2), and
827 SNr (D2), which are also structures innervated by DRN *Pet1*⁺ neurons (B1, C1, and D1).
828 *Pdyn*⁺*Pet1*⁺ axons were not found in structures that were functionally distant from basal
829 ganglia circuits, such as dLGN (E2) and hypothalamic nuclei (F2), although these structures
830 received dense inputs from DRN *Pet1*⁺ neurons (E1 and F1). Regions outlined in yellow in B1
831 – F1 are enlarged in the insets showing EGFP⁺ / tdTomato⁺ axon fibers in each region.
832 Abbreviations: DRN – dorsal raphe nucleus. VP – ventral pallidum. EP – entopeduncular
833 nucleus. SNr – substantia nigra pars reticulata. dLGN – dorsal lateral geniculate nucleus. LH –
834 lateral hypothalamus. VMH – ventromedial hypothalamus. All tissue sections are
835 counterstained with fluorescent Neurotrace (Nissl).
836

SUPPLEMENTARY INFORMATION

Table S1: Genes for identification of major cell types.

Figure S1 (related to Figure 1)

Comparison of cell type composition across sample batches and sex.

(A) t-SNE plot of the dataset with cells color-coded by experiment batch. All clusters contain cells from both batches.

(B) t-SNE plot of the dataset with cells color-coded by the sex of the mouse from which the sample was acquired.

(C) Bar plots showing the percentage of cells in each batch (left) or sex (right) that are categorized into each of the 17 major cell types.

Figure S2 (related to Figure 1)

Ependymal cells lining the ventral cerebral aqueduct are of several distinct subtypes.

(A) t-SNE plots of the dataset, with cells color-coded by their expression of genes identifying different subsets of ependymal cell. *Hdc* is expressed in all ependymal cells, whereas genes such as *Cdhr4*, *Ucma*, and *Pdyn* are expressed in distinct subsets.

(B) Images of coronal *ISH* from the Allen Brain Atlas showing expression of *Hdc* and *Pdyn* at various parts of the ventricular system. *Hdc* is expressed by ependymal cells lining most of the ventricular system. *Pdyn* expression is specific to the cells lining the ventromedial part of the posterior ventricular system, where it is highly expressed in the cerebral aqueduct, but not the lateral ventricles or 3rd ventricle.

Figure S3 (related to Figure 3)

Enriched gene ontology terms associated with genes differentially expressed between 5-HT neuron subtypes.

Selected gene ontology (GO) terms that were significantly enriched ($Q < 0.05$, Benjamini-Hochberg correction) were sorted by ontology category and arranged in order of increasing Q values. Q values and the proportion of differentially expressed genes associated with each GO term, expressed as a percentage of genes in the background list associated with the GO term, are shown as bar plots. The majority of genes differentially expressed between 5-HT neuron subtypes were membrane proteins (GO:0016020, 193 of 333 genes) that included transporters, cell adhesion molecules, receptors, and synaptic proteins.

Figure S4 (related to Figure 4)

Processing of *ISH* images for spatial correlation analysis.

(A) Overview of workflow for processing *ISH* images from the Allen Brain Atlas to generate the spatial expression matrix. Coronal images spanning the DRN in each *ISH* experiment were downsampled and centered on the brain slice. The midline in each slice was identified and the image was rotated to align the midline vertically. Rotated images were cropped and assigned to corresponding positions along the anterior-posterior axis relative to the Allen Brain Atlas coronal template. Cells positive for the *ISH* signal were identified using a spot detection algorithm and counted in 50 x 50 μm bins to generate 2D histograms for each image. 2D histograms, representing the spatial expression profile of the probed gene in a given coronal section, were aligned and cropped along the dorsal-ventral axis to retain only the region containing the DRN (36 X bins x 36 Y bins). Cropped histograms were averaged with the left-

884 right reflection and combined with the other histograms generated from other images in the
885 same experiment image series to generate the volume data (36 X bins x 36 Y bins x 12
886 images) including NaN values for missing data. Volume data for each gene was unrolled into a
887 single row vector (of 15,552 entries), and row vectors were concatenated to generate the
888 spatial expression matrix for spatial correlation analysis.

889 **(B)** Sum of 2D histograms generated by the workflow in (A), displayed as a series of 12
890 coronal sections showing the summed count of cells detected across all *ISH* images analyzed.
891 Anatomical landmarks such as the cerebral aqueduct, fiber tracts, periaqueductal gray, and
892 DRN are easily discerned from the images of the histograms, suggesting that the histograms
893 were well aligned and have good coverage of the DRN.

894 **(C)** Plot of the number of genes used for the spatial correlation analysis at each of the 12
895 coronal sections (genes per 2D histogram). Genes with missing data at a given coronal section
896 (i.e. no image or damaged slice) were not included in the count. Approximately 80 genes were
897 used for calculating the correlation coefficient for each spatial bin.

898 **(D)** Scatter plot of the total expression and mean-normalized variance for genes in the spatial
899 expression matrix within the *Tph2*⁺ region. Each dot represents 1 of the 123 genes in the
900 expression matrix. Genes with low spatial variability within the masked region, such as *Tph2*
901 (marked red), and low total expression were excluded from the spatial correlation analysis.
902 *Met*, which showed the most spatial variability since its expression is restricted to the posterior
903 cluster, is also marked on the plot.

904

905

Figure S5 (related to Figure 4)

Correlation coefficient maps for DRN 5-HT neuron subtypes.

Spatial correlation maps displayed as heatmaps arranged in columns for each 5-HT neuron subtype. Heatmaps correspond to coronal sections, and are arranged vertically in order along the anterior-posterior axis. The averaged *Tph2* ISH signal is included in the left-most column as a reference for the DRN outline. Spatial bins in the heatmaps with positive correlations (green) indicate the most likely locations of each 5-HT neuron subtype. Spatial correlation maps have been smoothed using a 2D Gaussian filter (1SD) for visualization. Since only differentially expressed genes were used for this analysis, negative correlations are also seen. These reflect the locations of 5-HT neurons of other subtypes from which, by definition, the differentially expressed genes that define one subtype are excluded. Scale bars: 500 μ m.

Figure S6 (related to Figure 5)

Caudal DRN B7 neurons innervate ventral striatum and prefrontal cortex

Distributions of Str-projecting (A), NAc-projecting (B), and mPFC-projecting (C) neurons displayed as probability density maps overlaid on the Allen Brain Atlas coronal template. Str-projecting and NAc-projecting are both found in the dorsomedial DRN at anterior sections (columns 1 – 2). Str-projecting neurons are more restricted to anterior sections of the DRN, whereas the NAc-projecting neurons are also found in posterior sections of the DRN (columns 3 – 5) where they overlap with the distribution of mPFC-projecting neurons.

Figure S7 (related to Figure 5)

Spatial distributions of projection-defined subpopulations

Distributions of all projection-defined subpopulations in Fig. 5 displayed as probability density maps. Distributions for each subpopulation were projected onto either the horizontal or sagittal planes (50 x 100 μ m bins). The midline in horizontal projections is indicated by a straight gray line at 0 mm, and distances from the midline are negative for the hemisphere ipsilateral to the injection site. The region occupied by the cerebral aqueduct is shaded in solid gray in sagittal projections, and the depth indicated is relative to the origin of the PIR space in the Allen Brain Atlas. The flattened projection of the region containing *Tph2*⁺ cells is outlined by the gray dashed line in each image. Str-projecting and GPe-projecting subpopulations were the most similar, whereas the Str-projecting and NAc-projecting subpopulations were mostly overlapping in the anterior DRN but differed in the posterior DRN. Cells outside of the ventrolateral periaqueductal gray and DRN, such as cells in the pedunclopontine nucleus or dorsal periaqueductal gray, were excluded from the probability maps. Abbreviations: Str: striatum; GPe: globus pallidus, external; NAc: nucleus accumbens; LHA: lateral hypothalamic area; M1: primary motor cortex; mPFC: medial prefrontal cortex; dLGN: dorsal lateral geniculate nucleus; Hb: habenula.

Figure S8 (related to Figure 5)

Ventrolateral DRN neurons send axon collaterals to both striatum and motor cortex.

(A) Schematic of double retrograde tracing experiment using unpseudotyped rabies viruses. RbV-tdTomato was injected into primary motor cortex, and RbV-EGFP was injected into the ipsilateral striatum. Tissue collection for histology was performed 7 days post-injection.

(B) Representative fluorescent image of a coronal section through the anterior DRN containing both M1- and Str-projecting neurons. 5-HT neurons were labeled by an antibody stain for TPH2. Neurons innervating both M1 and Str were co-labeled by RbV-tdTomato and RbV-EGFP, and were typically found in the ventrolateral DRN and the dorsal border of the ventromedial DRN. Inset (i) is a confocal image of the ventrolateral DRN region in (B) marked by the white dashed box, and inset (ii) is a confocal image of the ventromedial DRN region in (B) marked by the yellow dashed box. Both insets are centered on TPH2⁺ cells co-labeled by RbV-tdTomato and RbV-EGFP.

Figure S9 (related to Figure 6)

Quantification of RNAscope puncta in Str-projecting neurons.

Scatter plots with marginal histograms showing the quantification of the number of single molecular FISH puncta (analyzed by RNAscope) in each Str-projecting cell. Each dot represents a single RbV-labeled cell. RbV-labeled cells were categorized based on expression of *Slc6a4* and one of four 5-HT subtype candidate markers gene: *Pdyn* (A) for 5-HT-III, *Slc17a8* (B) and *Cbln2* (C) for 5-HT-IV, and *Trh* (D) for 5-HT-I. Dashed lines in the scatter plots and marginal histograms indicate the thresholds used to binarize expression. Separate RNAscope experiments were performed for each 5-HT subtype candidate marker gene. All RbV-labeled cells in the analyzed images were included, including some cells in the pedunculopontine nucleus, and the number of RbV-labeled cells in each experiment is indicated in the plot.

Figure S10 (related to Figure 7)

***Pet1*⁺;*Pdyn*⁺ neurons innervate a subset of regions targeted by DRN *Pet1*⁺ neurons.**

Images of cortical and subcortical regions in the forebrain from conditional anterograde tracing of axons from DRN *Pet1*⁺ neurons and *Pdyn*⁺;*Pet1*⁺ neurons. Axons from *Pdyn*⁺;*Pet1*⁺ neurons were also found in frontal and prefrontal cortical regions (A-B), but were absent from thalamic nuclei that were innervated by DRN *Pet1*⁺ neurons (D-G) and subcortical regions outside of the basal ganglia, such as SC (H). Within Str, *Pdyn*⁺;*Pet1*⁺ neurons were not uniformly distributed, with the highest density in the ventrolateral regions of Str. Abbreviations: ACC: anterior cingulate cortex; M1: primary motor cortex; S1: primary somatosensory cortex; Str: striatum; Sub: submedial thalamic nucleus; Re: nucleus reuniens; Hb: habenula; PF: parafascicular thalamic nucleus; MGN: medial geniculate nucleus; APT: anterior pretectal nucleus; SC: superior colliculus. Scale bars: 500 μ m.

MATERIALS AND METHODS

Mice

The following mouse strains/lines were used in this study: C57BL/6J (The Jackson Laboratory, Stock # 000664), *Pet1-Cre* (The Jackson Laboratory, Stock # 012712), *Pet1-Flpe* (from the lab of Susan Dymecki (Jensen et al., 2008)), *Pdyn-IRES-Cre* (The Jackson Laboratory, Stock # 027958), and *R26-LSL-FSF-ReaChR:mCitrine* (The Jackson Laboratory, Stock # 024846). Animals were kept on a 12:12 regular light/dark cycle under standard housing conditions. All procedures were performed in accordance with protocols approved by the Harvard Standing Committee on Animal Care following guidelines described in the U.S. National Institutes of Health Guide for the Care and Use of Laboratory Animals.

Adeno-Associated Viruses (AAVs)

Recombinant AAVs used for anterograde tracing experiments (AAV2/1-CAG-FLEX-EGFP, AAV2/1-CAG-FLEX-tdTomato) were commercially obtained from the Penn Vector Core. Virus aliquots were stored at -80 °C, and were injected at a concentration of approximately 10^{12} GC/ml.

Rabies Viruses

Rabies viruses used for retrograde tracing (B19G-SADΔG-EGFP, B19G-SADΔG-tdTomato) were generated in-house (Osakada and Callaway, 2013; Wickersham et al., 2010). Virions were amplified from existing stocks in several rounds of low-MOI passaging through BHK-B19G cells by transferring filtered supernatant, with 3 to 4 days between passages a maximum of 3 passages. Cells were grown at 35 °C and 5% CO₂ in DMEM with GlutaMAX (Thermo

Scientific, #10569010) supplemented with 5% heat-inactivated FBS (Thermo Scientific #10082147) and antibiotic-antimycotic (Thermo Scientific #15240-062). Media containing virions were collected at the end of the last passaging round and with benzonase nuclease (1:1000, Millipore #70664) at 37°C for 30 min, followed by filtration through a 0.22 µm PES filter. Filtered supernatant was transferred to ultracentrifuge tubes (Beckman Coulter #344058) with 2 ml of a 20% sucrose in dPBS cushion and ultracentrifugated at 20,000 RPM (Beckman Coulter SW 32 Ti rotor) at 4°C for 2 hours. The supernatant was discarded and the pellet was resuspended in dPBS for 6 hours on an orbital shaker at 4 °C before aliquots were prepared and frozen for long-term storage at -80 °C. Unpseudotyped rabies virus titers were estimated using a serial dilution method counting infected HEK 293T cells and quantified as infectious units per ml (IU/ml).

Stereotaxic Surgeries

Mice were initially anesthetized with 5% isoflurane (80% oxygen) and maintained at 1-2.5% isoflurane after placement on the stereotaxic frame (David Kopf Instruments, Model 1900 Stereotaxic Alignment System). The scalp was cleaned and sterilized before an incision was made to expose the skull, and sterile ophthalmic ointment was applied to the eyes. For leveling the horizontal plane, a stereotaxic alignment tool (David Kopf Instruments, Model 1905) was used to zero the relative dorsoventral displacement of Bregma and Lambda, as defined in the Paxinos & Franklin Mouse Brain Atlas (Paxinos and Franklin, 2001), for adjusting tilt of the anterior-posterior axis, and of two points equidistant to the left and right of Bregma for adjusting the tilt of the medial-lateral axis. Craniotomies were prepared using a mounted drill (David Kopf Instruments, Model 1911) with careful removal of the bone flap and overlying dura

using forceps and a fine needle tip, and were covered with sterile 0.9% saline before and during the injection to prevent desiccation. Viruses were front-filled into a pulled glass pipette (Drummond Scientific, #5-000-2005) filled with mineral oil (Millipore Sigma, M3516) and connected to a 5 μ l Hamilton syringe (Hamilton #84850) via polyethylene tubing filled with mineral oil. Glass pipettes were pulled to obtain a tip size of approximately 40-60 μ m on a pipette puller (Sutter Instrument Co., P-97). Viruses were infused into target regions at approximately 100 nl/min using a syringe pump (Harvard Apparatus, #883015), and pipettes were slowly withdrawn ($< 10 \mu\text{m/s}$) at least 10 min after the end of the infusion. Following wound closure, mice were placed in a cage with a heating pad until their activity was recovered before returning to their home cage. Mice were given pre- and post-operative oral carprofen (MediGel CPF, 5mg/kg/day) as an analgesic, and monitored daily for at least 4 days post-surgery.

Stereotaxic Injection Coordinates and Volumes

All coordinates are relative to Bregma along the anterior-posterior axis and medial-lateral axis, and relative to the pial surface along the dorsoventral axis. “BL” denotes the distance between Bregma and Lambda. Angles for DV coordinates are relative to the dorsoventral axis along the sagittal plane, with 0° being a straight vertical approach and negative values denoting a posterior-to-anterior approach. Dorsal raphe nucleus (DRN): AP = $-(6.25 * \text{BL} / 4.35)$ mm, ML = 0.00 mm, DV = -3.33 mm at -40°, 200-300 nl. Ventrolateral striatum (vlStr): AP = +0.40 mm, ML = ± 2.45 mm, DV = -3.10 mm at 0°, 300 nl. Dorsal lateral geniculate nucleus (dLGN): AP = $-(2.00 * \text{BL} / 4.20)$ mm, ML = ± 2.25 mm, DV = -3.00 mm at 0°, 150 nl. Globus pallidus, external (GPe): AP = +0.14 mm, ML = ± 2.34 mm, DV = -3.90 mm at 0°, 200 nl. Lateral hypothalamic

area (LHA): AP = -1.46 mm, ML = ± 1.10 mm, DV = -5.10 mm at 0°, 150 nl. Habenula (Hb): AP = -(1.30 * BL / 4.2) mm, ML = ± 0.43 mm, DV = -2.80 mm at 0°, 50 nl. Nucleus accumbens core (NAcc): AP = +1.54 mm, ML = ± 1.10 mm, DV = -4.00 mm at 0°, 300 nl. Primary motor cortex (M1), 6 sites: AP = {+2.10 mm, +1.60 mm, +1.10 mm}, ML = { ± 1.75 mm, ± 1.60 mm, ± 1.60 mm}, DV = {[-1.20 mm, -0.60 mm], [-1.10 mm, -0.50 mm], [-1.00 mm, -0.40 mm]} at 0°, 150 nl per site. Medial prefrontal cortex (mPFC), 4 sites: AP = {+2.4 mm, +1.8 mm}, ML = ± 0.40 mm, DV = {-1.65 mm, -1.25 mm} at 0°, 150 nl per site.

Single Cell Dissociation and RNA Sequencing

8- to 10-week old C57BL/6J mice were pair-housed in a regular 12:12 light/dark cycle room prior to tissue collection. Mice were transcardially perfused with an ice-cold choline cutting solution containing neuronal activity blockers (110 mM choline chloride, 25 mM sodium bicarbonate, 12 mM D-glucose, 11.6 mM sodium L-ascorbate, 10 mM HEPES, 7.5 mM magnesium chloride, 3.1 mM sodium pyruvate, 2.5 mM potassium chloride, 1.25 mM sodium phosphate monobasic, 10 μ M (R)-CPP, 1 μ M tetrodotoxin, saturated with bubbling 95% oxygen/5% carbon dioxide, pH adjusted to 7.4 using sodium hydroxide). Brains were rapidly dissected out and sliced into 250 μ m thick coronal sections on a vibratome (Leica Biosystems, VT1000) in a chilled cutting chamber filled with choline cutting solution. Coronal slices containing the DRN were then transferred to a chilled dissection dish containing a choline-based cutting solution for microdissection. Fiber tracts were used for guiding the microdissection but were excluded from the collected tissue chunk. Dissected tissue chunks were transferred to cold HBSS-based dissociation media (Thermo Fisher Scientific Cat. # 14170112, supplemented to final content concentrations: 138 mM sodium chloride, 11 mM D-

1078 glucose, 10 mM HEPES, 5.33 mM potassium chloride, 4.17 mM sodium bicarbonate, 2.12 mM
1079 magnesium chloride, 0.9 mM kynurenic acid, 0.441 mM potassium phosphate monobasic,
1080 0.338 mM sodium phosphate monobasic, 10 μ M (R)-CPP, 1 μ M tetrodotoxin, saturated with
1081 bubbling 95% oxygen/5% carbon dioxide, pH adjusted to 7.35 using sodium hydroxide)
1082 supplemented with an additional inhibitor cocktail (10 μ M triptolide, 5 μ g/ml actinomycin D, 30
1083 μ g/ml anisomycin) and kept on ice until dissections were completed. Dissected tissue chunks
1084 for each sample were pooled into a single tube for the subsequent dissociation steps. Tissue
1085 chunks were first mixed with a digestion cocktail (dissociation media, supplemented to working
1086 concentrations: 20 U/ml papain, 1 mg/ml pronase, 0.05 mg/mL DNase I, 10 μ M triptolide, 5
1087 μ g/ml actinomycin D, 30 μ g/ml anisomycin) and incubated at 34 °C for 90 min with gentle
1088 rocking. The digestion was quenched by adding dissociation media supplemented with 0.2%
1089 BSA and 10 mg/ml ovomucoid inhibitor (Worthington Cat. # LK003128), and samples were
1090 kept chilled for the rest of the dissociation procedure. Digested tissue was collected by brief
1091 centrifugation (5 min, 300 g), re-suspended in dissociation media supplemented with 0.2%
1092 BSA, 1 mg/ml ovomucoid inhibitor, and 0.05 mg/mL DNase I. Tissue chunks were then
1093 mechanically triturated using fine-tip plastic micropipette tips of progressively decreasing size.
1094 The triturated cell suspension was filtered in two stages using a 70 μ m cell strainer (Miltenyi
1095 Biotec Cat # 130-098-462) and 40 μ m pipette tip filter (Bel-Art Cat. # H136800040) and
1096 washed in two repeated centrifugation (5 min, 300 g) and re-suspension steps to remove
1097 debris before a final re-suspension in dissociation media containing 0.04% BSA and 15%
1098 OptiPrep (Sigma D1556). Cell density was calculated based on hemocytometer counts and
1099 adjusted to approximately 100,000 cells/ml. Single-cell encapsulation and RNA capture on the
1100 InDrop platform was performed at the Harvard Medical School ICCB Single Cell Core using v3

chemistry hydrogels based on previously described protocols (Zilionis et al., 2017). Suspensions were kept chilled until the cells were flowed into the microfluidic device. Libraries were prepared and indexed following the protocols referenced above, and sequencing-ready libraries were stored at -80 °C. Libraries from different samples were pooled and sequenced on an Illumina NextSeq 500 (High Output v2 kits).

Sequencing Data Processing

NGS data was processed using previously a published pipeline in Python available at <https://github.com/indrops/indrops> (Klein et al., 2015). Briefly, reads were filtered by expected structure and sorted by the corresponding library index. Valid reads were then demultiplexed and sorted by cell barcodes. Cell barcodes containing fewer than 250 total reads were discarded, and remaining reads were aligned to a reference mouse transcriptome (Ensembl GRCm38 release 87) using Bowtie 1.2.2 (m = 200, n = 1, l = 15, e = 100). For alignment, the mouse transcriptome was modified with the addition of genes from the SAD B19 rabies viruses and transgenes (*B19N*, *B19P*, *B19M*, *B19L*, *EGFP*, *tdTomato*, *AmCyan1*). Aligned reads were then quantified as UMI-filtered mapped read (UMIFM) counts. UMIFM counts and quantification metrics for each cell were combined into a single file sorted by library and exported as a gunzipped TSV file.

Pre-Clustering Filtering and Normalization

Analysis of the processed NGS data was performed in R (version 3.4.4) using the Seurat package (version 2.3.1) (Butler et al., 2018; Satija et al., 2015). A custom R script was used to combine the expression data and metadata from all libraries corresponding to a single batch,

and cells with fewer than 500 UMIFM counts were removed. The expression data matrix (Genes x Cells) was filtered to retain genes with > 5 UMIFM counts, and then loaded into a Seurat object along with the library metadata for downstream processing. The percentage of mitochondrial transcripts for each cell (percent.mito) was calculated and added as metadata to the Seurat object. Cells in the object were further filtered using the following parameters: Reads – min. 20000, max. Inf; nUMI – min. 500, max. 18000; nGene – min. 200, max. 6000; percent.mito – min. -Inf, max. 0.1. Low quality libraries identified as outliers on scatter plots of quality control metrics (e.g. unusually low gradient on the nGene vs. nUMI) were also removed from the dataset. Filtered Seurat objects were then log-normalized at 10,000 transcripts per cell. Effects of latent variables (nUMI, percent.mito, Sex, orig.ident) were estimated and regressed out using a GLM (ScaleData function, model.use = “linear”), and the scaled and centered residuals were used for dimensionality reduction and clustering.

Dimensionality Reduction and Batch Effect Correction

Canonical correlation analysis (CCA) was used for dimensionality reduction and mitigation of batch effects. We used the union of the top 2000 highly variable genes from each batch dataset (3341 genes) and used the RunCCA function in Seurat to calculate 50 canonical variates (CVs). After inspection of the CVs, the first 35 CVs were used for subspace alignment when merge datasets from different batches into a single Seurat object. Cells with expression profiles not well explained by CVs (var.ratio.pca < 0.5) were removed from the dataset before clustering.

Cell Clustering and Cluster Identification

Initial clustering was performed on the merged and CCA-aligned dataset using the first 35 CVs, and t-SNE was used only for data visualization. Clustering was run using the SNN-based `FindClusters` function using the SLM algorithm and 10 iterations. Clustering was performed at varying resolution values, and we chose a final value of 2 for the resolution parameter for this stage of clustering. Clusters were assigned preliminary identities based on expression of combinations of known marker genes for major cell classes and types. A list genes used for identifying major cell classes and types is provided in Supplementary Table 1. Low quality cells were identified based on a combination of low gene/UMIFM counts and high levels of mitochondrial and nuclear transcripts (e.g. *Malat1*, *Meg3*, *Kcnq1ot1*) typically clustered together and were removed. Following assignment of preliminary identities, cells were divided into data subsets as separate Seurat objects (neurons, astrocytes, ependymal cells, vascular cells, immune cells, oligodendrocytes and polydendrocytes) for further subclustering. The expression matrix for each data subset was further filtered to include only genes expressed by the cells in the subset (minimum cell threshold of 0.5% of cells in the subset). Subclustering was performed iteratively on each data subset to resolve additional cell types and subtypes. Briefly, clustering was run at high resolution, and the resulting clusters were ordered in a cluster dendrogram built using the Ward2 method in `hclust` using cluster-averaged gene expression for calculating the Euclidean distance matrix. Putative doublets/multiplets were identified based on co-expression of known marker genes for different cell types (e.g. neuronal and glial markers, or endothelial cell and pericyte markers). Putative doublets tended to separate from other cells and cluster together, and these clusters were removed from the dataset. Cluster separation was evaluated using the `AssessNodes` function

and inspection of differentially expressed genes at each node. Clusters with poor separation, based on high OOB scores and differential expression of mostly housekeeping genes, were merged to avoid over-separation of the data. The dendrogram was reconstructed after merging or removal of clusters, and the process of inspecting and merging or removing clusters was repeated until all resulting clusters could be distinguished based on a set of differentially expressed genes that we could validate separately. For small clusters that were previously identified in preliminary analysis of the separate batches, such as the *Met*-expressing 5-HT neuron subtype, or expected clusters based on existing literature, such as the *Slc17a8⁺;Fev⁻* neurons, manual identification and clustering was performed if these cells were not separated by the clustering algorithm.

Differential Expression Tests

Tests for differential gene expression were performed using MAST (version 1.4.1) through the `FindMarkersNode` function in Seurat (`logfc.threshold = 0.25`, `min.pct = 0.1`). P values were corrected using the Benjamini-Hochberg method and filtered a 5% false discovery rate ($Q < 0.05$).

Gene Ontology Term Enrichment Tests

GO term enrichment tests were performed using the `goseq` package (version 1.30.0) in R. Genes differentially expressed between 5-HT neuron subtypes were used as the target list, and all genes expressed in the 5-HT neuron dataset were used for the background list. Enrichment scores were calculated using the Wallenius approximation method in `goseq`, and

terms were filtered using Q values at a 5% false discovery rate (Benjamini-Hochberg correction).

Spatial Correlation Analysis

Spatial correlation analysis was performed in MATLAB (MathWorks, R2016b and R2018b). A spatial expression matrix for the differentially expressed (DE) genes was constructed using *in situ* hybridization images from the Allen Brain Atlas. Only DE genes with coronal imaging data were included in the matrix to achieve sufficient resolution along the dorsal-ventral and medial-lateral axes. For each gene, ISH images spanning the DRN were downsampled by a factor of 2 before registration and expression quantification using a custom MATLAB script. The midline of each slice was vertically aligned and centered, and images were and cropped to retain a region spanning approximately 1 mm across the midline containing the DRN. Cropped images were each assigned to a position along the anterior-posterior axis corresponding to a coronal section from the Allen Brain Atlas averaged coronal template (100 μ m intervals). Expression was binarized by thresholding the image, and positive cells were detected using a Laplacian-of-Gaussian spot detection algorithm. Spatial expression patterns were obtained from two-dimensional histograms (bin size = 50 μ m x 50 μ m) of positive cells counts in each slice. Fine alignment of each 2D histogram along the dorsal-ventral axis was adjusted manually using *Tph2* ISH images as the reference. Anatomical landmarks visible in the Nissl or background stain, such as the cerebral aqueduct and fiber tracts, were used for the fine adjustment. Aligned histograms were cropped to retain a square region (36 bins x 36 bins) containing the DRN. Cropped 2D histograms were averaged with the left-right reflection, and the ISH count data for each experiment (36 bins x 36 bins x 12 sections) was unrolled into a row vector. Row

vectors for the same gene were averaged, ignoring NaN values from missing ISH data, to obtain a single row vector for each gene. Row vectors for each gene were concatenated to generate the spatial expression matrix. The spatial expression matrix (Genes x Bins) was further filtered in two stages: bins with no *Tph2* expression were removed, and genes were filtered based on total expression and mean-normalized variance (Fig. S5). Pearson correlation coefficients were calculated between the averaged gene expression of each 5-HT neuron subtype cluster from the scRNA-seq dataset and each spatial bin in the filtered spatial expression matrix.

Histology for Anatomical Tracing

Mice were deeply anesthetized with isoflurane and transcardially perfused with 5-10 ml chilled 0.1 M PBS, followed by 10-15 ml chilled 4% paraformaldehyde in 0.1 M PBS. Brains were dissected out and post-fixed overnight at 4 °C, followed by incubation in a storing/cryoprotectant solution of 30% sucrose and 0.05% sodium azide in 0.1 M PBS for at least 1-2 days to equilibrate. 50 µm coronal slices were prepared on a freezing microtome (Leica Biosystems, SM2010 R). Slices were either immunostained (see section on Immunohistochemistry), or counterstained using Neurotrace 435 (ThermoFisher Scientific N21479) at a concentration of 1:100 in 0.1 M PBS with 0.5% Triton X-100. Slices were mounted in VectaShield mounting media (Vector Labs, H-1000) and imaged on an Olympus VS120 slide scanning microscope. Confocal images were taken on an Olympus FV1000 or FV1200 confocal microscope for assessing co-localization.

Immunohistochemistry

50 µm thick free-floating tissue sections were rinsed 3 x 5 min with 0.1 M PBS containing 0.5% Triton X-100 (PBST) and blocked in a PBST-based solution containing 6% normal goat serum for 1 hour at room temperature. The blocking solution was then removed, and slices were incubated overnight at 4 °C in a PBST-based antibody carrier solution containing 3% normal goat serum and rabbit anti-TPH2 primary antibodies (Millipore, ABN60) diluted 1:1000. After incubation in the primary antibody carrier solution, slices were rinsed 4 x 5 min with PBST, and then incubated in carrier solution containing goat anti-rabbit Alexa Fluor 647 at 1:500 (ThermoFisher Scientific, A-21244) and Neurotrace 435 at 1:100 for 2 hours at room temperature. Slices were then rinsed 2 x 5 min in PBST and 2 x 5 min in PBS before mounting with VectaShield mounting media (Vector Labs, H-1000).

Fluorescent *In Situ* Hybridization (FISH)

Animals were deeply anesthetized with isoflurane before decapitation. Brains then were rapidly removed, frozen on dry ice, and embedded in tissue freezing media (Tissue-Tek O.C.T. compound). 20 µm coronal sections were prepared on a cryostat (Leica Biosystems, CM1950) and mounted onto SuperFrost Plus glass slides (VWR) at 100 µm intervals between slices in a set. Slices were rapidly refrozen once mounted, and stored at -80 °C before staining. Multiplexed fluorescent *in situ* hybridization was performed using the ACDBio RNAscope V1 reagents and protocols. Briefly, slices were fixed in 4% paraformaldehyde at 4 °C for 15 minutes and dehydrated through washing steps in ethanol at increasing concentrations (50%, 70%, 100%) before protease digestion (Protease III, 10 minutes at room temperature). Probes and amplification/detection reagents were applied to the tissue sections and incubated under

conditions stated in the V1 detection protocol provided by ACDBio. Sections were counterstained using DAPI provided in the V1 detection reagent kits and mounted in ProLong Gold mounting media (ThermoFisher Scientific P36934). Single-plane tiled images covering the DRN were scanned using a confocal microscope (Leica SP8X, 1.40 NA 63X magnification oil immersion objective). Tile merging was performing in the Leica LAS X software, with a 10% tile overlap and statistical blending.

FISH Image Analysis

Confocal images were first processed in FIJI. A custom macro was written to convert Leica image files (.lif format) into TIFF format for downstream analysis steps. Channels in the merged tile images were processed separately. For each channel, a median filter (1 pixel radius) was applied before images were cropped and downsampled by a factor of 2 with bicubic interpolation. A rolling ball background subtraction (50 pixel radius) was then applied before images for each channel was saved as a separate 8-bit TIFF file. A pixel classifier run in Ilastik (version 1.2.2) was applied on the output TIFF files to generate probability maps of *B19N*-expressing cell bodies for automated segmentation of rabies-infected cells. Cell segmentation and RNAscope puncta quantification was performed using a custom pipeline in CellProfiler (version 3.1.5). Puncta counts were exported as TSV files for further analysis and data visualization using custom scripts written in R and MATLAB.

1282 **Data Availability**

1283 R data files containing the single cell transcriptional data in the form of Seurat objects and
 1284 annotations were uploaded onto the Harvard Dataverse
 1285 ([https://dataverse.harvard.edu/privateurl.xhtml?token=12575c44-cec4-4cd6-af5c-](https://dataverse.harvard.edu/privateurl.xhtml?token=12575c44-cec4-4cd6-af5c-fe111e3d4ed6)
 1286 [fe111e3d4ed6](https://dataverse.harvard.edu/privateurl.xhtml?token=12575c44-cec4-4cd6-af5c-fe111e3d4ed6)).

REFERENCES

- Azmitia, E.C., and Segal, M. (1978). An autoradiographic analysis of the differential ascending projections of the dorsal and median raphe nuclei in the rat. *J Comp Neurol* 179, 641–667.
- Banasr, M., Hery, M., Printemps, R., and Daszuta, A. (2004). Serotonin-induced increases in adult cell proliferation and neurogenesis are mediated through different and common 5-HT receptor subtypes in the dentate gyrus and the subventricular zone. *Neuropsychopharmacology* 29, 450–460.
- Bang, S.J., Jensen, P., Dymecki, S.M., and Commons, K.G. (2012). Projections and interconnections of genetically defined serotonin neurons in mice. *Eur J Neurosci* 35, 85–96.
- Brisch, R., Steiner, J., Mawrin, C., Krzyżanowska, M., Jankowski, Z., and Gos, T. (2017). Microglia in the dorsal raphe nucleus plays a potential role in both suicide facilitation and prevention in affective disorders. *Eur Arch Psychiatry Clin Neurosci* 267, 403–415.
- Bromberg-Martin, E.S., Hikosaka, O., and Nakamura, K. (2010). Coding of task reward value in the dorsal raphe nucleus. *J Neurosci* 30, 6262–6272.
- Butler, A., Hoffman, P., Smibert, P., Papalexi, E., and Satija, R. (2018). Integrating single-cell transcriptomic data across different conditions, technologies, and species. *Nat. Biotechnol.*
- Calabresi, P., Picconi, B., Tozzi, A., Ghiglieri, V., and Di Filippo, M. (2014). Direct and indirect pathways of basal ganglia: a critical reappraisal. *Nat Neurosci* 17, 1022–1030.
- Calizo, L.H., Akanwa, A., Ma, X., Pan, Y.-Z., Lemos, J.C., Craige, C., Heemstra, L.A., and Beck, S.G. (2011). Raphe serotonin neurons are not homogenous: electrophysiological, morphological and neurochemical evidence. *Neuropharmacology* 61, 524–543.
- Chen, K.H., Boettiger, A.N., Moffitt, J.R., Wang, S., and Zhuang, X. (2015). Spatially resolved, highly multiplexed RNA profiling in single cells. *Science* 348, aaa6090.
- Cohen, J.Y., Amoroso, M.W., and Uchida, N. (2015). Serotonergic neurons signal reward and punishment on multiple timescales. *Elife* 4, 463.
- Colgan, L.A., Cavolo, S.L., Commons, K.G., and Levitan, E.S. (2012). Action potential-independent and pharmacologically unique vesicular serotonin release from dendrites. *J Neurosci* 32, 15737–15746.
- Commons, K.G. (2015). Two major network domains in the dorsal raphe nucleus. *J Comp Neurol* 523, 1488–1504.
- Cools, R., Roberts, A.C., and Robbins, T.W. (2008). Serotonergic regulation of emotional and behavioural control processes. *Trends Cogn Sci (Regul Ed)* 12, 31–40.
- Dahlström, A., and Fuxe, K. (1964). Localization of monoamines in the lower brain stem. *Experientia* 20, 398–399.

de Kock, C.P.J., Cornelisse, L.N., Burnashev, N., Lodder, J.C., Timmerman, A.J., Couey, J.J.,
Mansvelder, H.D., and Brussaard, A.B. (2006). NMDA receptors trigger neurosecretion of 5-HT
within dorsal raphe nucleus of the rat in the absence of action potential firing. *The Journal of
Physiology* 577, 891–905.

Deneris, E., and Gaspar, P. (2018). Serotonin neuron development: shaping molecular and
structural identities. *Wiley Interdiscip Rev Dev Biol* 7.

Di Matteo, V., Pierucci, M., Esposito, E., Crescimanno, G., Benigno, A., and Di Giovanni, G.
(2008). Serotonin modulation of the basal ganglia circuitry: therapeutic implication for
Parkinson's disease and other motor disorders. *Prog Brain Res* 172, 423–463.

Dölen, G., Darvishzadeh, A., Huang, K.W., and Malenka, R.C. (2013). Social reward requires
coordinated activity of nucleus accumbens oxytocin and serotonin. *Nature* 501, 179–184.

Economo, M.N., Clack, N.G., Lavis, L.D., Gerfen, C.R., Svoboda, K., Myers, E.W., and
Chandrashekar, J. (2016). A platform for brain-wide imaging and reconstruction of individual
neurons. *Elife* 5, e10566.

Fenno, L.E., Mattis, J., Ramakrishnan, C., Hyun, M., Lee, S.Y., He, M., Tucciarone, J.,
Selimbeyoglu, A., Berndt, A., Grosenick, L., et al. (2014). Targeting cells with single vectors
using multiple-feature Boolean logic. *Nat Meth* 11, 763–772.

Ferguson, J.M. (2001). SSRI Antidepressant Medications: Adverse Effects and Tolerability.
Prim Care Companion J Clin Psychiatry 3, 22–27.

Fernandez, S.P., Cauli, B., Cabezas, C., Muzerelle, A., Poncer, J.-C., and Gaspar, P. (2015).
Multiscale single-cell analysis reveals unique phenotypes of raphe 5-HT neurons projecting to
the forebrain. *Brain Struct Funct* 221, 1–19.

Fisone, G., Snyder, G.L., Fryckstedt, J., Caplan, M.J., Aperia, A., and Greengard, P. (1995).
Na⁺,K⁺-ATPase in the choroid plexus. Regulation by serotonin/protein kinase C pathway. *J.
Biol. Chem.* 270, 2427–2430.

Fu, W., Le Maître, E., Fabre, V., Bernard, J.-F., David Xu, Z.-Q., and Hökfelt, T. (2010).
Chemical neuroanatomy of the dorsal raphe nucleus and adjacent structures of the mouse
brain. *J Comp Neurol* 518, 3464–3494.

Gagnon, D., and Parent, M. (2014). Distribution of VGLUT3 in highly collateralized axons from
the rat dorsal raphe nucleus as revealed by single-neuron reconstructions. *PLoS ONE* 9,
e87709.

Gartlehner, G., Hansen, R.A., Morgan, L.C., Thaler, K., Lux, L., Van Noord, M., Mager, U.,
Thieda, P., Gaynes, B.N., Wilkins, T., et al. (2011). Comparative benefits and harms of
second-generation antidepressants for treating major depressive disorder: an updated meta-
analysis. *Ann. Intern. Med.* 155, 772–785.

Gong, H., Xu, D., Yuan, J., Li, X., Guo, C., Peng, J., Li, Y., Schwarz, L.A., Li, A., Hu, B., et al.

(2016). High-throughput dual-colour precision imaging for brain-wide connectome with cytoarchitectonic landmarks at the cellular level. *Nature Communications* 7, 12142.

Grailhe, R., Grabtree, G.W., and Hen, R. (2001). Human 5-HT(5) receptors: the 5-HT(5A) receptor is functional but the 5-HT(5B) receptor was lost during mammalian evolution. *Eur. J. Pharmacol.* 418, 157–167.

Granger, A.J., Wallace, M.L., and Sabatini, B.L. (2017). Multi-transmitter neurons in the mammalian central nervous system. *Current Opinion in Neurobiology* 45, 85–91.

Hale, M.W., and Lowry, C.A. (2011). Functional topography of midbrain and pontine serotonergic systems: implications for synaptic regulation of serotonergic circuits. *Psychopharmacology* 213, 243–264.

Hall, I.C., Rebec, G.V., and Hurley, L.M. (2010). Serotonin in the inferior colliculus fluctuates with behavioral state and environmental stimuli. *J. Exp. Biol.* 213, 1009–1017.

Haugas, M., Tikker, L., Achim, K., Salminen, M., and Partanen, J. (2016). Gata2 and Gata3 regulate the differentiation of serotonergic and glutamatergic neuron subtypes of the dorsal raphe. *Development* 143, 4495–4508.

Hayashi, K., Nakao, K., and Nakamura, K. (2015). Appetitive and aversive information coding in the primate dorsal raphe nucleus. *J Neurosci* 35, 6195–6208.

Hintiryan, H., Foster, N.N., Bowman, I., Bay, M., Song, M.Y., Gou, L., Yamashita, S., Bienkowski, M.S., Zingg, B., Zhu, M., et al. (2016). The mouse cortico-striatal projectome. *Nat Neurosci* 19, 1100–1114.

Hioki, H., Nakamura, H., Ma, Y.-F., Konno, M., Hayakawa, T., Nakamura, K.C., Fujiyama, F., and Kaneko, T. (2010). Vesicular glutamate transporter 3-expressing nonserotonergic projection neurons constitute a subregion in the rat midbrain raphe nuclei. *J Comp Neurol* 518, 668–686.

Hornung, J.-P. (2010). The Neuroanatomy of the Serotonergic System. In *Handbook of the Behavioral Neurobiology of Serotonin*, C.P. Müller, and B.L. Jacobs, eds. (Elsevier), pp. 51–64.

Howerton, A.R., Roland, A.V., and Bale, T.L. (2014). Dorsal raphe neuroinflammation promotes dramatic behavioral stress dysregulation. *J Neurosci* 34, 7113–7123.

Hrvatin, S., Hochbaum, D.R., Nagy, M.A., Cicconet, M., Robertson, K., Cheadle, L., Zilionis, R., Ratner, A., Borges-Monroy, R., Klein, A.M., et al. (2018). Single-cell analysis of experience-dependent transcriptomic states in the mouse visual cortex. *Nat Neurosci* 21, 120–129.

Huot, P., Fox, S.H., and Brotchie, J.M. (2011). The serotonergic system in Parkinson's disease. *Prog. Neurobiol.* 95, 163–212.

Jacobs, B.L., and Fornal, C.A. (1997). Serotonin and motor activity. *Current Opinion in*

Neurobiology 7, 820–825.

Jensen, P., Farago, A.F., Awatramani, R.B., Scott, M.M., Deneris, E.S., and Dymecki, S.M. (2008). Redefining the serotonergic system by genetic lineage. *Nat Neurosci* 11, 417–419.

Kaushalya, S.K., Desai, R., Arumugam, S., Ghosh, H., Balaji, J., and Maiti, S. (2008). Three-photon microscopy shows that somatic release can be a quantitatively significant component of serotonergic neurotransmission in the mammalian brain. *J. Neurosci. Res.* 86, 3469–3480.

Kawashima, T., Zwart, M.F., Yang, C.-T., Mensh, B.D., and Ahrens, M.B. (2016). The Serotonergic System Tracks the Outcomes of Actions to Mediate Short-Term Motor Learning. *Cell* 167, 933–946.e20.

Klein, A.M., Mazutis, L., Akartuna, I., Tallapragada, N., Veres, A., Li, V., Peshkin, L., Weitz, D.A., and Kirschner, M.W. (2015). Droplet barcoding for single-cell transcriptomics applied to embryonic stem cells. *Cell* 161, 1187–1201.

Lee, S.-B., Lee, H.S., and Waterhouse, B.D. (2008). The collateral projection from the dorsal raphe nucleus to whisker-related, trigeminal sensory and facial motor systems in the rat. *Brain Res* 1214, 11–22.

Lein, E.S., Hawrylycz, M.J., Ao, N., Ayres, M., Bensinger, A., Bernard, A., Boe, A.F., Boguski, M.S., Brockway, K.S., Byrnes, E.J., et al. (2007). Genome-wide atlas of gene expression in the adult mouse brain. *Nature* 445, 168–176.

Li, Y., Zhong, W., Wang, D., Feng, Q., Liu, Z., Zhou, J., Jia, C., Hu, F., Zeng, J., Guo, Q., et al. (2016). Serotonin neurons in the dorsal raphe nucleus encode reward signals. *Nature Communications* 7, 10503.

Lowry, C.A. (2002). Functional subsets of serotonergic neurones: implications for control of the hypothalamic-pituitary-adrenal axis. *J. Neuroendocrinol.* 14, 911–923.

Lowry, C.A., Rodda, J.E., Lightman, S.L., and Ingram, C.D. (2000). Corticotropin-releasing factor increases in vitro firing rates of serotonergic neurons in the rat dorsal raphe nucleus: evidence for activation of a topographically organized mesolimbocortical serotonergic system. *J Neurosci* 20, 7728–7736.

Mahmood, T., and Silverstone, T. (2001). Serotonin and bipolar disorder. *J Affect Disord* 66, 1–11.

Marcinkiewicz, C.A., Mazzone, C.M., D'Agostino, G., Halladay, L.R., Hardaway, J.A., DiBerto, J.F., Navarro, M., Burnham, N., Cristiano, C., Dorrier, C.E., et al. (2016). Serotonin engages an anxiety and fear-promoting circuit in the extended amygdala. *Nature* 537, 97–101.

Marques, S., Zeisel, A., Codeluppi, S., van Bruggen, D., Mendanha Falcão, A., Xiao, L., Li, H., Häring, M., Hochgerner, H., Romanov, R.A., et al. (2016). Oligodendrocyte heterogeneity in the mouse juvenile and adult central nervous system. *Science* 352, 1326–1329.

- 1427 Matias, S., Lottem, E., Dugue, G.P., and Mainen, Z.F. (2017). Activity patterns of serotonin
1428 neurons underlying cognitive flexibility. *Elife* 6, 365.
- 1429 Meltzer, H.Y., and Massey, B.W. (2011). The role of serotonin receptors in the action of
1430 atypical antipsychotic drugs. *Curr Opin Pharmacol* 11, 59–67.
- 1431 Miguelez, C., Morera-Herreras, T., Torrecilla, M., Ruiz-Ortega, J.A., and Ugedo, L. (2014).
1432 Interaction between the 5-HT system and the basal ganglia: functional implication and
1433 therapeutic perspective in Parkinson's disease. *Front. Neural Circuits* 8, 21.
- 1434 Miyazaki, K., Miyazaki, K.W., and Doya, K. (2012). The role of serotonin in the regulation of
1435 patience and impulsivity. *Mol. Neurobiol.* 45, 213–224.
- 1436 Monti, J.M. (2010). The structure of the dorsal raphe nucleus and its relevance to the
1437 regulation of sleep and wakefulness. *Sleep Medicine Reviews* 14, 307–317.
- 1438 Moskowitz, M.A., Liebmann, J.E., Reinhard, J.F., and Schlosberg, A. (1979). Raphe origin of
1439 serotonin-containing neurons within choroid plexus of the rat. *Brain Res* 169, 590–594.
- 1440 Muzerelle, A., Scotto-Lomassese, S., Bernard, J.-F., Soiza-Reilly, M., and Gaspar, P. (2016).
1441 Conditional anterograde tracing reveals distinct targeting of individual serotonin cell groups
1442 (B5-B9) to the forebrain and brainstem. *Brain Struct Funct* 221, 535–561.
- 1443 Niederkofler, V., Asher, T.E., Okaty, B.W., Rood, B.D., Narayan, A., Hwa, L.S., Beck, S.G.,
1444 Miczek, K.A., and Dymecki, S.M. (2016). Identification of Serotonergic Neuronal Modules that
1445 Affect Aggressive Behavior. *Cell Rep* 17, 1934–1949.
- 1446 Okaty, B.W., Freret, M.E., Rood, B.D., Brust, R.D., Hennessy, M.L., deBairos, D., Kim, J.C.,
1447 Cook, M.N., and Dymecki, S.M. (2015). Multi-Scale Molecular Deconstruction of the Serotonin
1448 Neuron System. *Neuron* 1–42.
- 1449 Osakada, F., and Callaway, E.M. (2013). Design and generation of recombinant rabies virus
1450 vectors. *Nat Protoc* 8, 1583–1601.
- 1451 Pauls, D.L., Abramovitch, A., Rauch, S.L., and Geller, D.A. (2014). Obsessive-compulsive
1452 disorder: an integrative genetic and neurobiological perspective. *Nat Rev Neurosci* 15, 410–
1453 424.
- 1454 Paxinos, G., and Franklin, K.B.J. (2001). *The Mouse Brain in Stereotaxic Coordinates* (San
1455 Diego, California, USA: Academic Press).
- 1456 Pisanello, F., Sileo, L., Oldenburg, I.A., Pisanello, M., Martiradonna, L., Assad, J.A., Sabatini,
1457 B.L., and De Vittorio, M. (2014). Multipoint-Emitting Optical Fibers for Spatially Addressable
1458 In Vivo Optogenetics.
- 1459 Politis, M., and Niccolini, F. (2014). Serotonin in Parkinson's disease. *Behav Brain Res.*
- 1460 Poulin, J.-F., Caronia, G., Hofer, C., Cui, Q., Helm, B., Ramakrishnan, C., Chan, C.S.,

Dombeck, D.A., Deisseroth, K., and Awatramani, R. (2018). Mapping projections of molecularly defined dopamine neuron subtypes using intersectional genetic approaches. *Nat Neurosci* 21, 1260–1271.

Poulin, J.-F., Zou, J., Drouin-Ouellet, J., Kim, K.-Y.A., Cicchetti, F., and Awatramani, R.B. (2014). Defining midbrain dopaminergic neuron diversity by single-cell gene expression profiling. *Cell Rep* 9, 930–943.

Reed, M.C., Nijhout, H.F., and Best, J. (2013). Computational studies of the role of serotonin in the basal ganglia. *Front Integr Neurosci* 7, 41.

Ren, J., Friedmann, D., Xiong, J., Liu, C.D., Ferguson, B.R., Weerakkody, T., DeLoach, K.E., Ran, C., Pun, A., Sun, Y., et al. (2018). Anatomically Defined and Functionally Distinct Dorsal Raphe Serotonin Sub-systems. *Cell* 175, 472–487.e20.

Root, D.H., Zhang, S., Barker, D.J., Miranda-Barrientos, J., Liu, B., Wang, H.-L., and Morales, M. (2018). Selective Brain Distribution and Distinctive Synaptic Architecture of Dual Glutamatergic-GABAergic Neurons. *Cell Rep* 23, 3465–3479.

Satija, R., Farrell, J.A., Gennert, D., Schier, A.F., and Regev, A. (2015). Spatial reconstruction of single-cell gene expression data. *Nat. Biotechnol.* 33, 495–502.

Saunders, A., Macosko, E.Z., Wysocki, A., Goldman, M., Krienen, F.M., de Rivera, H., Bien, E., Baum, M., Bortolin, L., Wang, S., et al. (2018). Molecular Diversity and Specializations among the Cells of the Adult Mouse Brain. *Cell* 174, 1015–1030.e1016.

Schilman, E.A., Klavir, O., Winter, C., Sohr, R., and Joel, D. (2010). The role of the striatum in compulsive behavior in intact and orbitofrontal-cortex-lesioned rats: possible involvement of the serotonergic system. *Neuropsychopharmacology* 35, 1026–1039.

Steinbusch, H.W., Nieuwenhuys, R., Verhofstad, A.A., and van der Kooy, D. (1981). The nucleus raphe dorsalis of the rat and its projection upon the caudatoputamen. A combined cytoarchitectonic, immunohistochemical and retrograde transport study. *J. Physiol. (Paris)* 77, 157–174.

Templin, J.S., Bang, S.J., Soiza-Reilly, M., Berde, C.B., and Commons, K.G. (2012). Patterned expression of ion channel genes in mouse dorsal raphe nucleus determined with the Allen Mouse Brain Atlas. *Brain Res* 1457, 1–12.

Urban, D.J., Zhu, H., Marcinkiewicz, C.A., Michaelides, M., Oshibuchi, H., Rhea, D., Aryal, D.K., Farrell, M.S., Lowery-Gionta, E., Olsen, R.H.J., et al. (2016). Elucidation of The Behavioral Program and Neuronal Network Encoded by Dorsal Raphe Serotonergic Neurons. *Neuropsychopharmacology* 41, 1404–1415.

Van Bockstaele, E.J., Biswas, A., and Pickel, V.M. (1993). Topography of serotonin neurons in the dorsal raphe nucleus that send axon collaterals to the rat prefrontal cortex and nucleus accumbens. *Brain Res* 624, 188–198.

1497 Vanlandewijck, M., He, L., Mäe, M.A., Andrae, J., Ando, K., Del Gaudio, F., Nahar, K.,
1498 Lebouvier, T., Laviña, B., Gouveia, L., et al. (2018). A molecular atlas of cell types and
1499 zonation in the brain vasculature. *Nature Publishing Group* 554, 475–480.

1500 Vaswani, M., Linda, F.K., and Ramesh, S. (2003). Role of selective serotonin reuptake
1501 inhibitors in psychiatric disorders: a comprehensive review. *Prog Neuropsychopharmacol Biol*
1502 *Psychiatry* 27, 85–102.

1503 Vertes, R.P. (1991). A PHA-L analysis of ascending projections of the dorsal raphe nucleus in
1504 the rat. *J Comp Neurol* 313, 643–668.

1505 Wallace, M.L., Saunders, A., Huang, K.W., Philson, A.C., Goldman, M., Macosko, E.Z.,
1506 McCarroll, S.A., and Sabatini, B.L. (2017). Genetically Distinct Parallel Pathways in the
1507 Entopeduncular Nucleus for Limbic and Sensorimotor Output of the Basal Ganglia. *Neuron* 94,
1508 138–152.e5.

1509 Wang, X., Allen, W.E., Wright, M.A., Sylwestrak, E.L., Samusik, N., Vesuna, S., Evans, K., Liu,
1510 C., Ramakrishnan, C., Liu, J., et al. (2018). Three-dimensional intact-tissue sequencing of
1511 single-cell transcriptional states. *Science* 361.

1512 Waselus, M., Valentino, R.J., and Van Bockstaele, E.J. (2011). Collateralized dorsal raphe
1513 nucleus projections: a mechanism for the integration of diverse functions during stress. *J*
1514 *Chem Neuroanat* 41, 266–280.

1515 Waterhouse, B.D., Mihailoff, G.A., Baack, J.C., and Woodward, D.J. (1986). Topographical
1516 distribution of dorsal and median raphe neurons projecting to motor, sensorimotor, and visual
1517 cortical areas in the rat. *J Comp Neurol* 249, 460–76–478–81.

1518 Watkins, C.C., Sawa, A., and Pomper, M.G. (2014). Glia and immune cell signaling in bipolar
1519 disorder: insights from neuropharmacology and molecular imaging to clinical application.
1520 *Nature Publishing Group* 4, e350.

1521 Weissbourd, B., Ren, J., DeLoach, K.E., Guenther, C.J., Miyamichi, K., and Luo, L. (2014).
1522 Presynaptic partners of dorsal raphe serotonergic and GABAergic neurons. 83, 645–662.

1523 Wickersham, I.R., Sullivan, H.A., and Seung, H.S. (2010). Production of glycoprotein-deleted
1524 rabies viruses for monosynaptic tracing and high-level gene expression in neurons. *Nat Protoc*
1525 5, 595–606.

1526 Yokogawa, T., Hannan, M.C., and Burgess, H.A. (2012). The dorsal raphe modulates sensory
1527 responsiveness during arousal in zebrafish. *J Neurosci* 32, 15205–15215.

1528 Young, S.Z., Taylor, M.M., and Bordey, A. (2011). Neurotransmitters couple brain activity to
1529 subventricular zone neurogenesis. *Eur J Neurosci* 33, 1123–1132.

1530 Zeisel, A., Hochgerner, H., Lönnerberg, P., Johnsson, A., Memic, F., van der Zwan, J., Häring,
1531 M., Braun, E., Borm, L.E., La Manno, G., et al. (2018). Molecular Architecture of the Mouse
1532 Nervous System. *Cell* 174, 999–1014.e22.

1533 Zilionis, R., Nainys, J., Veres, A., Savova, V., Zemmour, D., Klein, A.M., and Mazutis, L.
1534 (2017). Single-cell barcoding and sequencing using droplet microfluidics. *Nat Protoc* 12, 44–
1535 73.

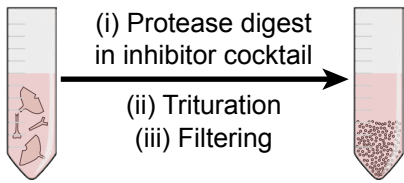
Figure 1

A

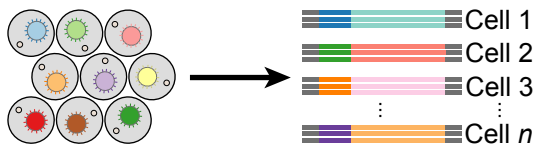
1. Sectioning & microdissection



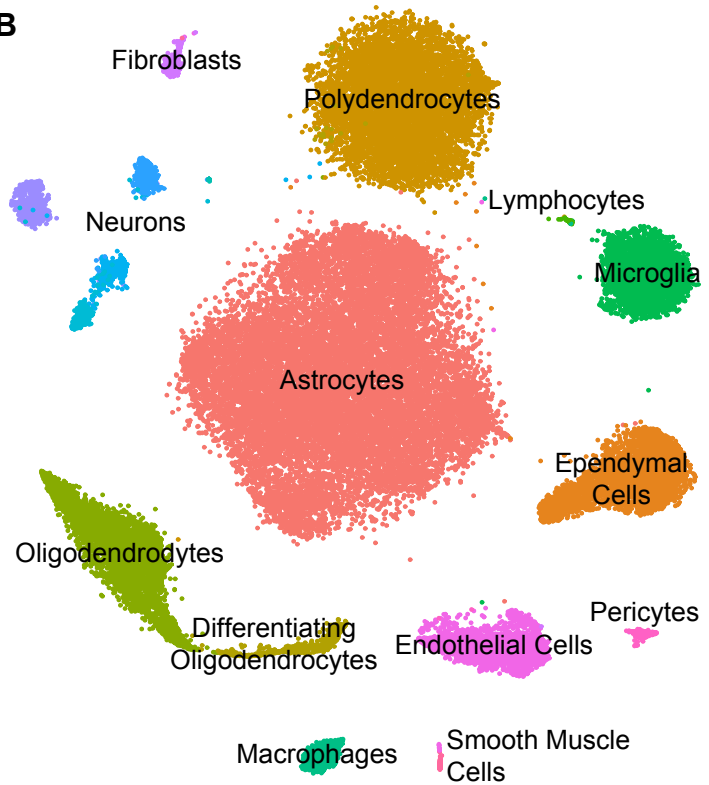
2. Digestion & dissociation



3. InDrop single-cell mRNA sequencing



B



C

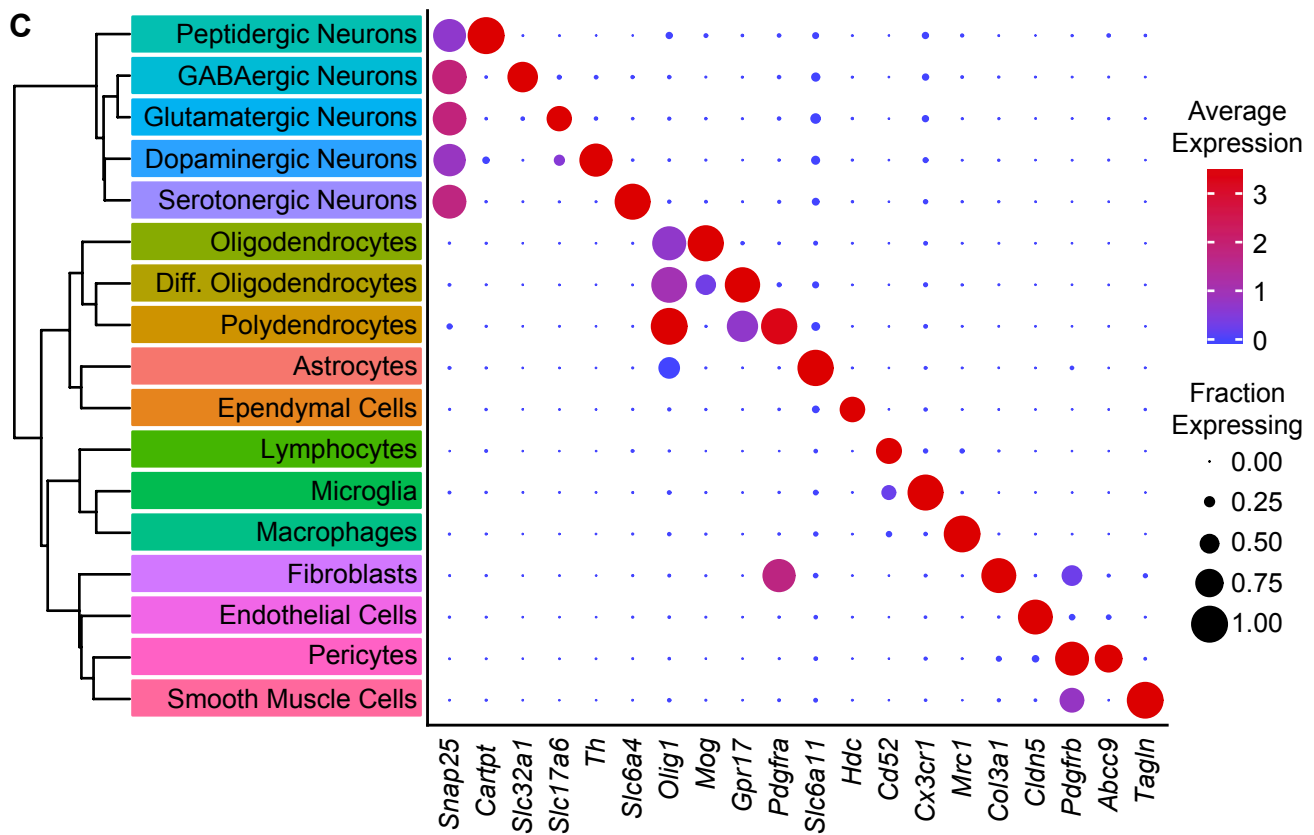


Figure 2

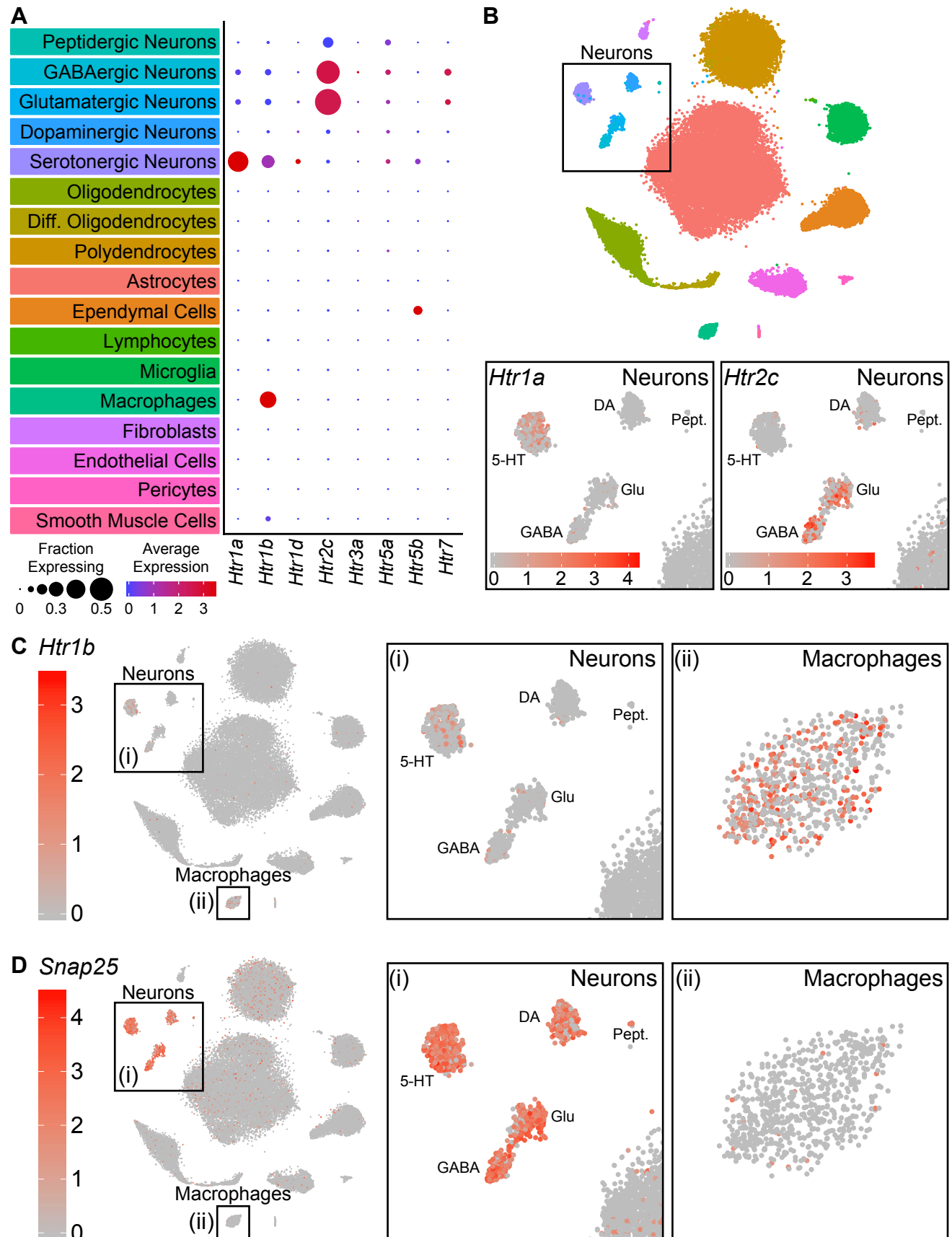


Figure 3

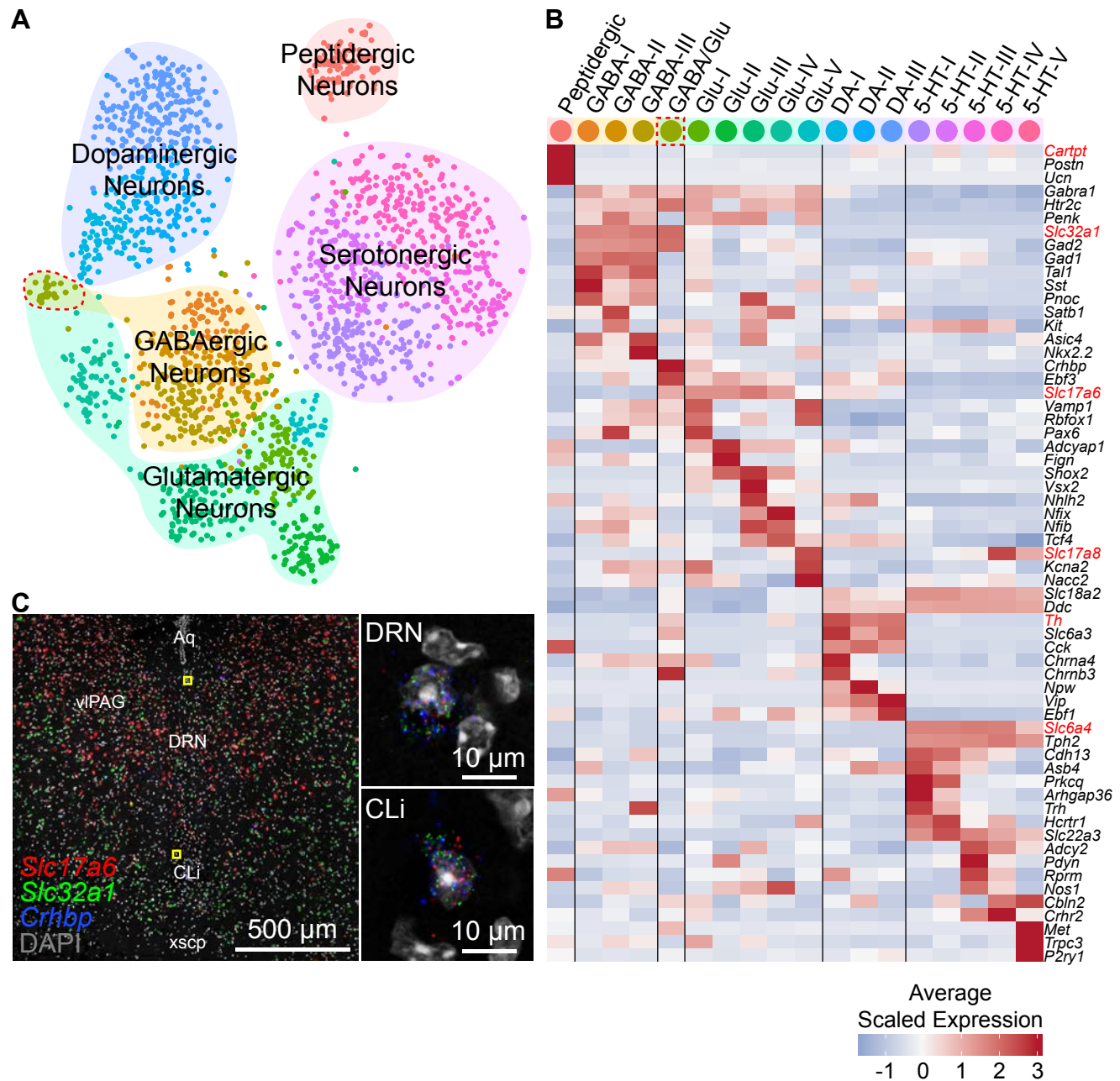


Figure 4

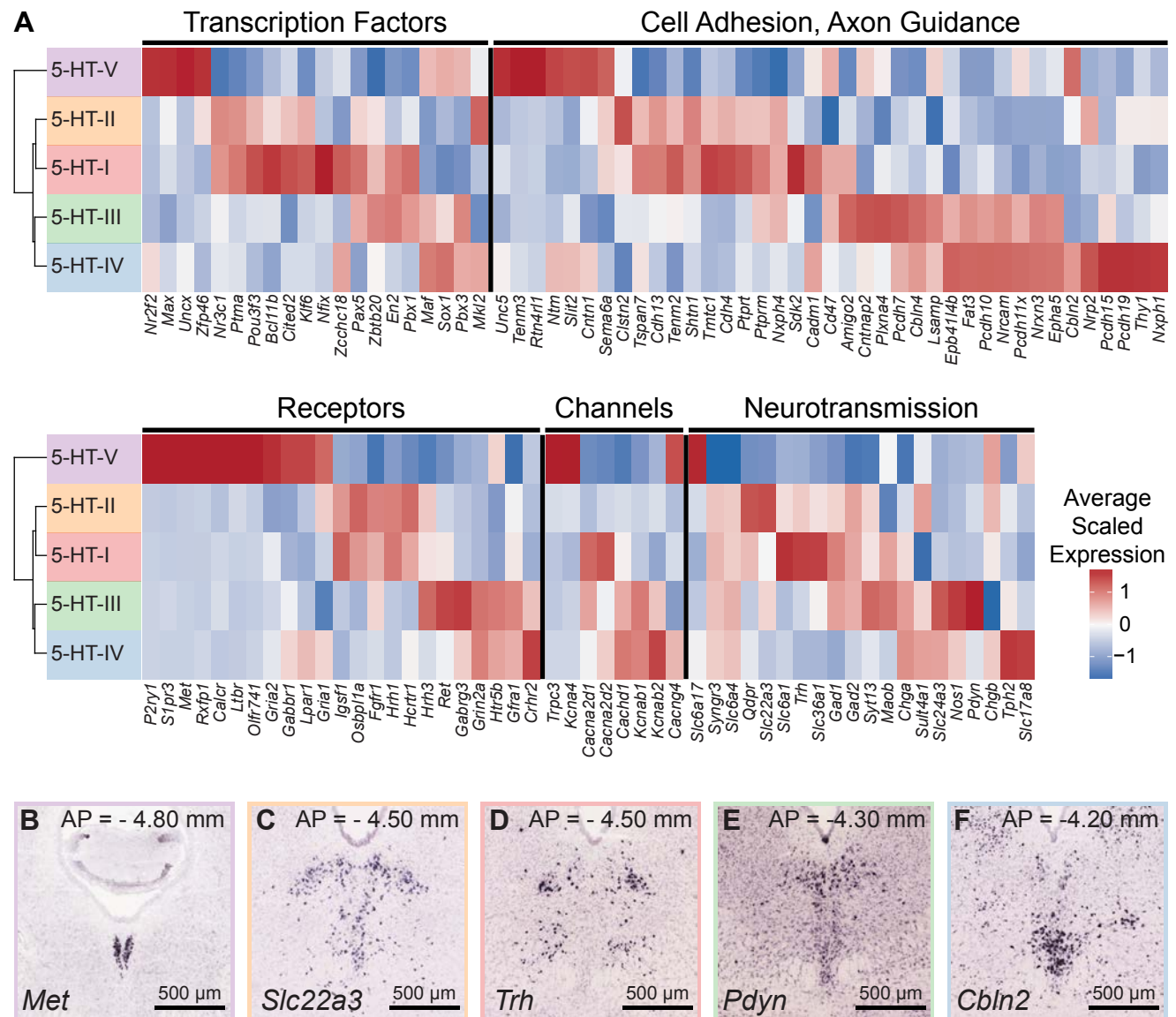


Figure 7

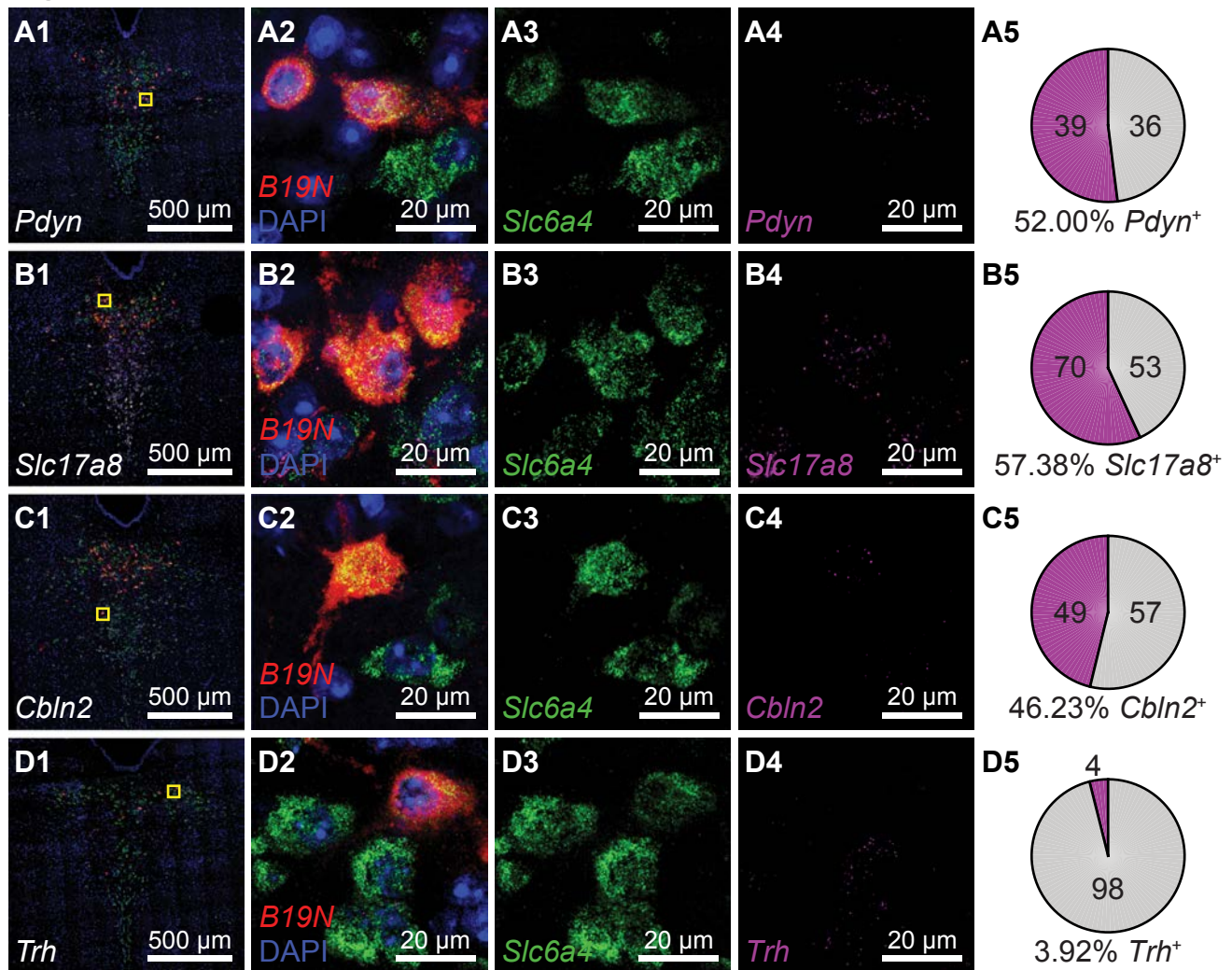


Figure 8

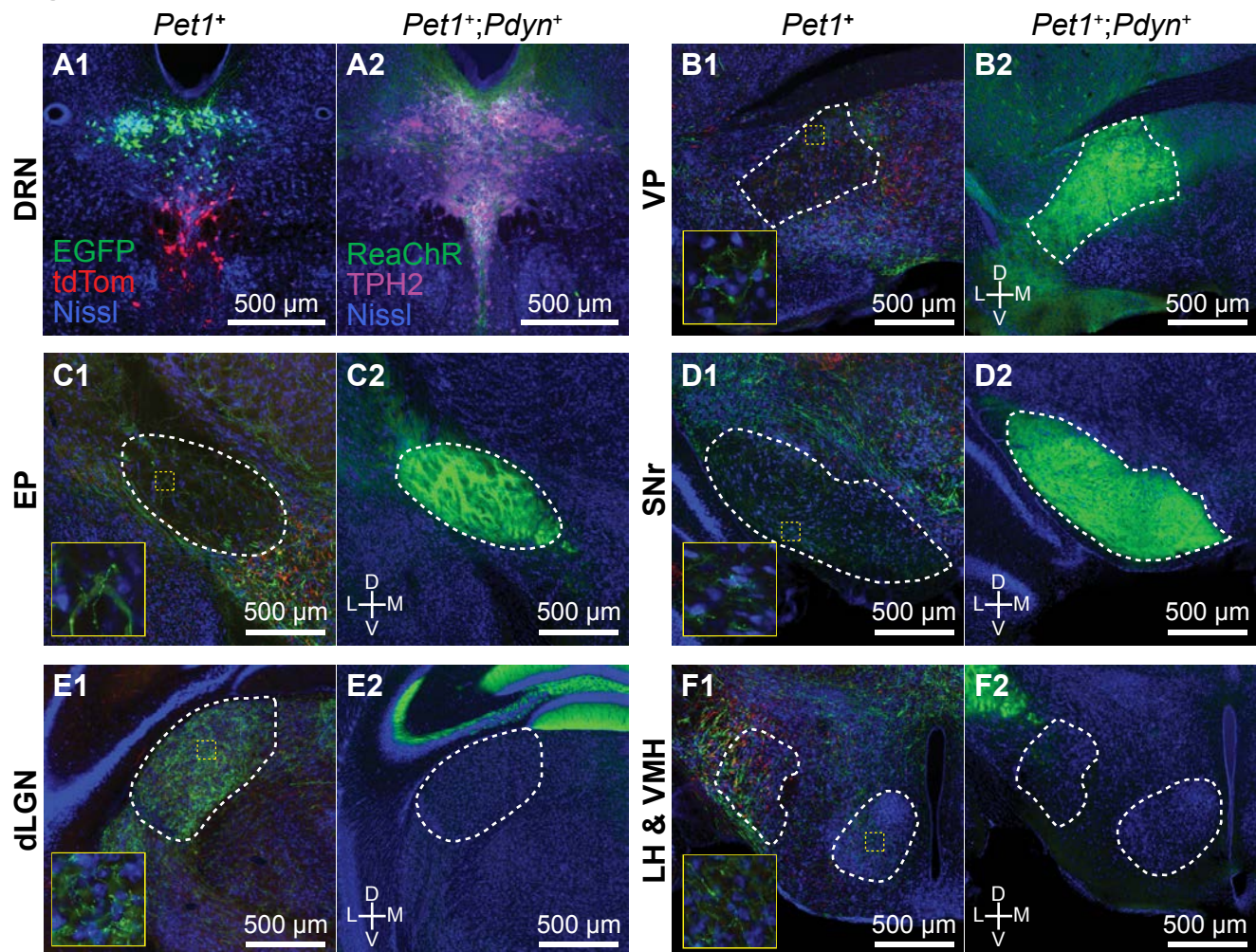


Figure S1

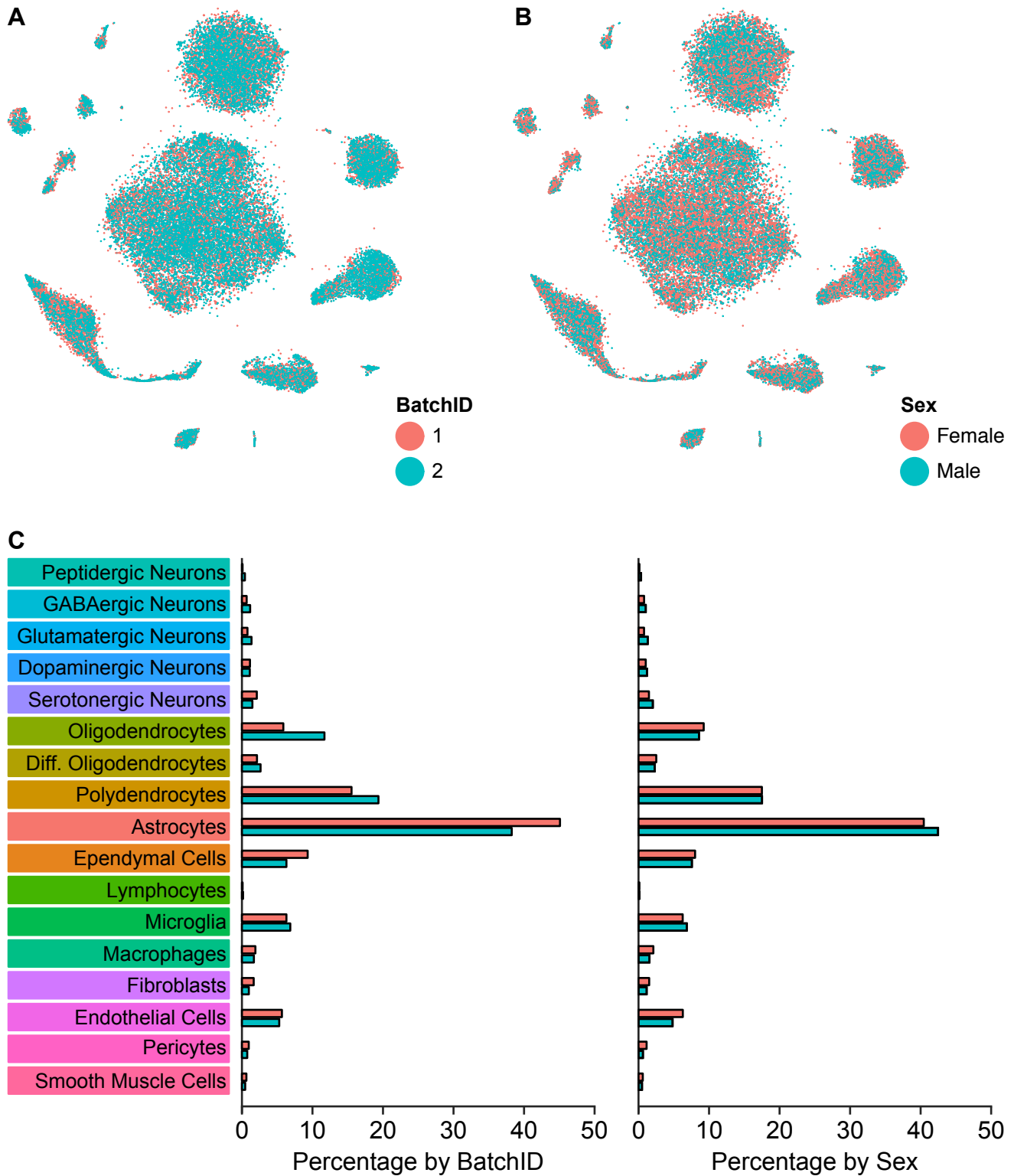


Figure S2

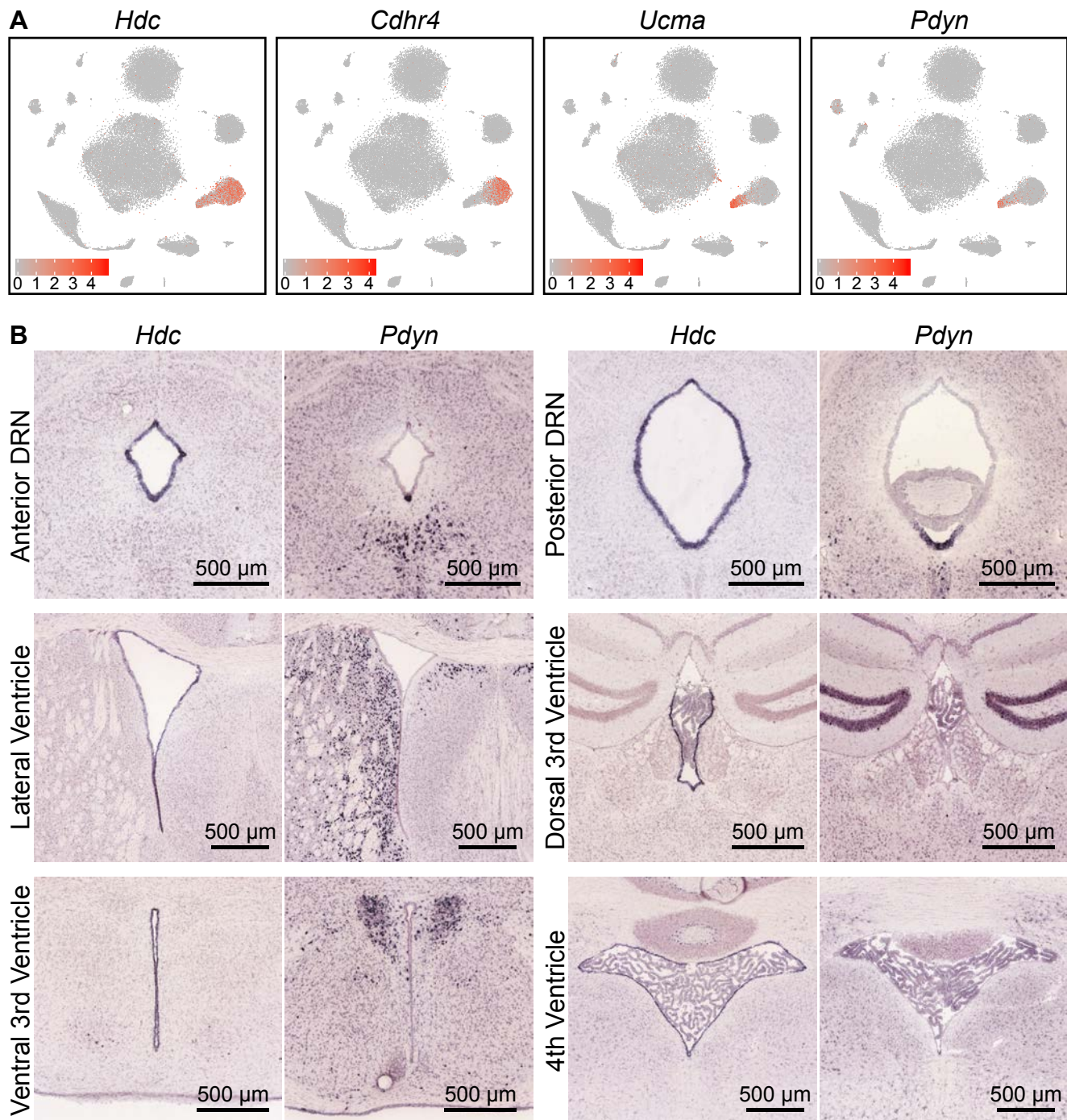


Figure S3

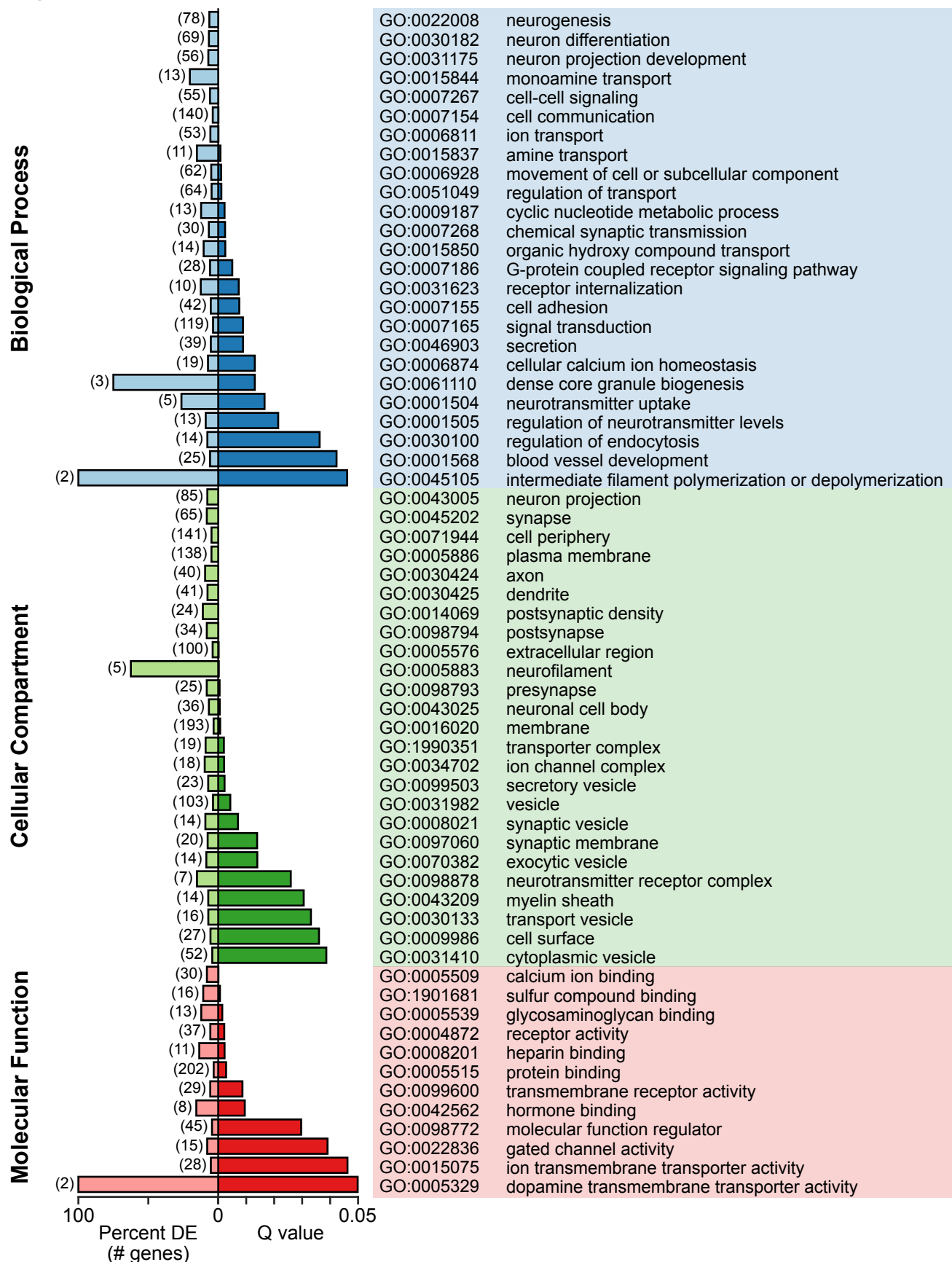


Figure S4

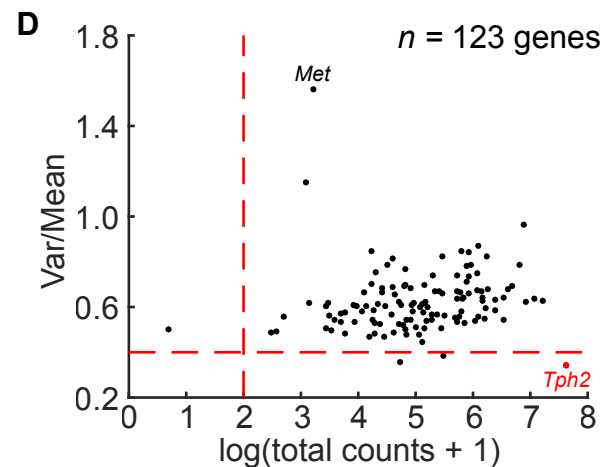
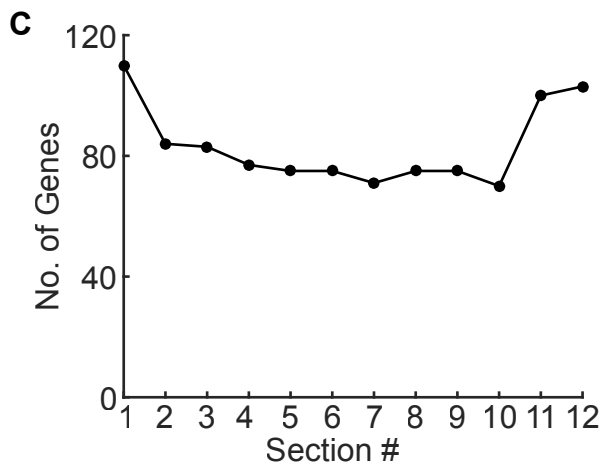
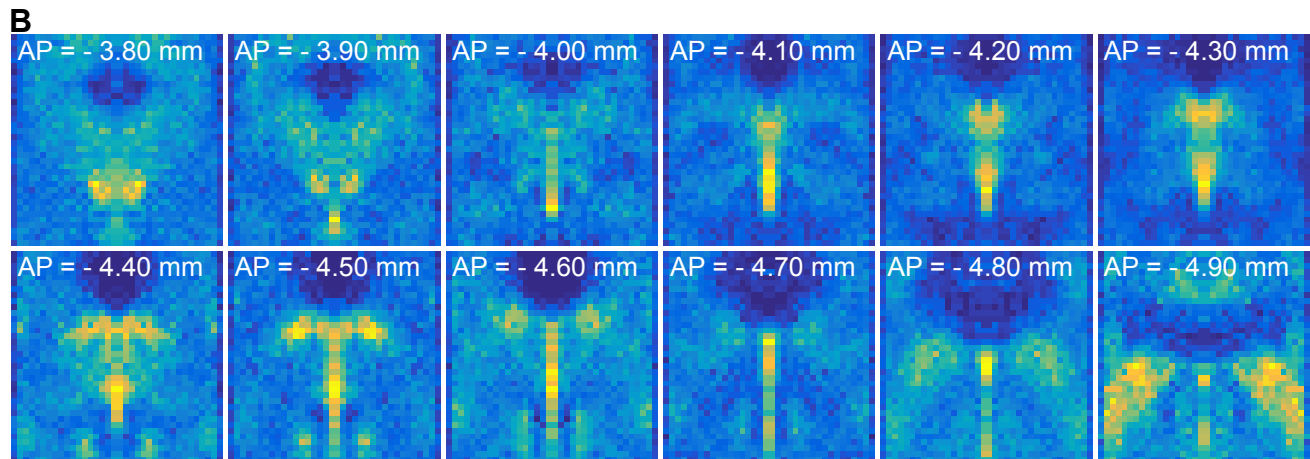
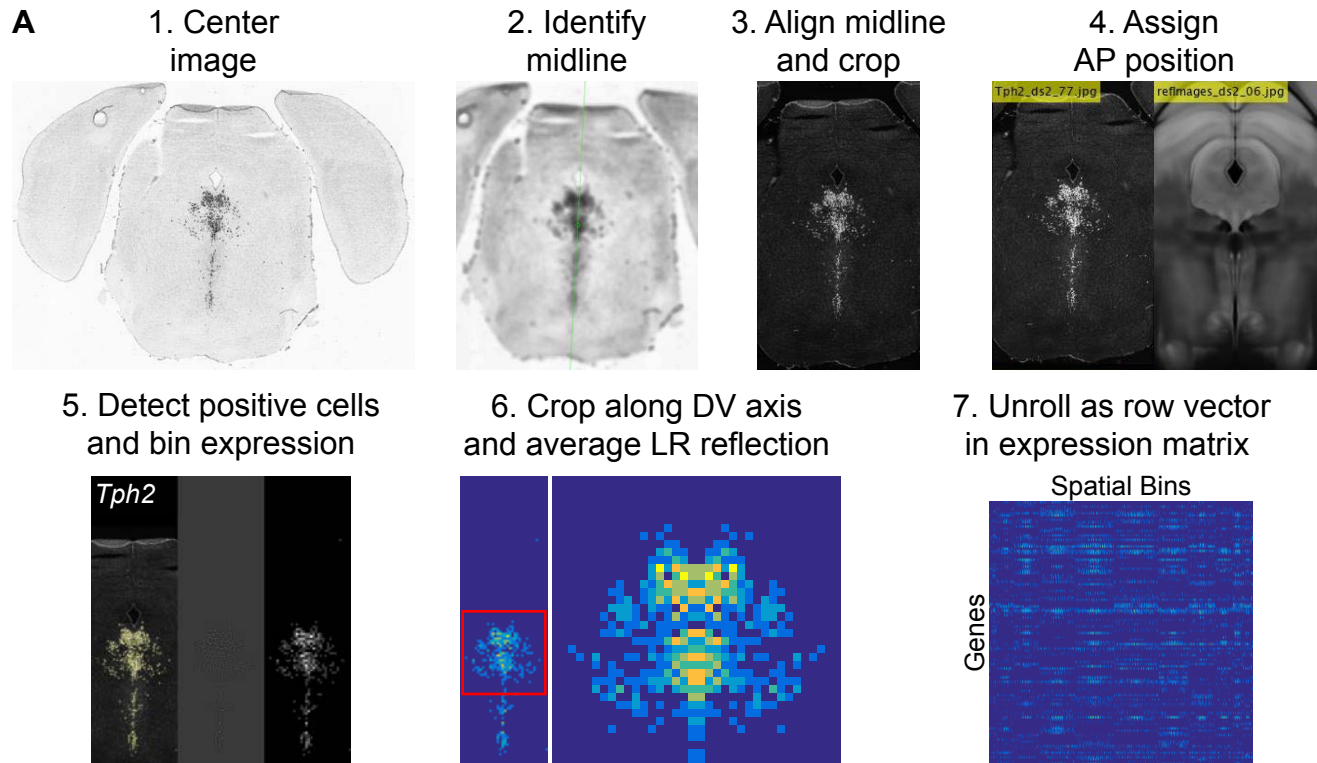


Figure S5

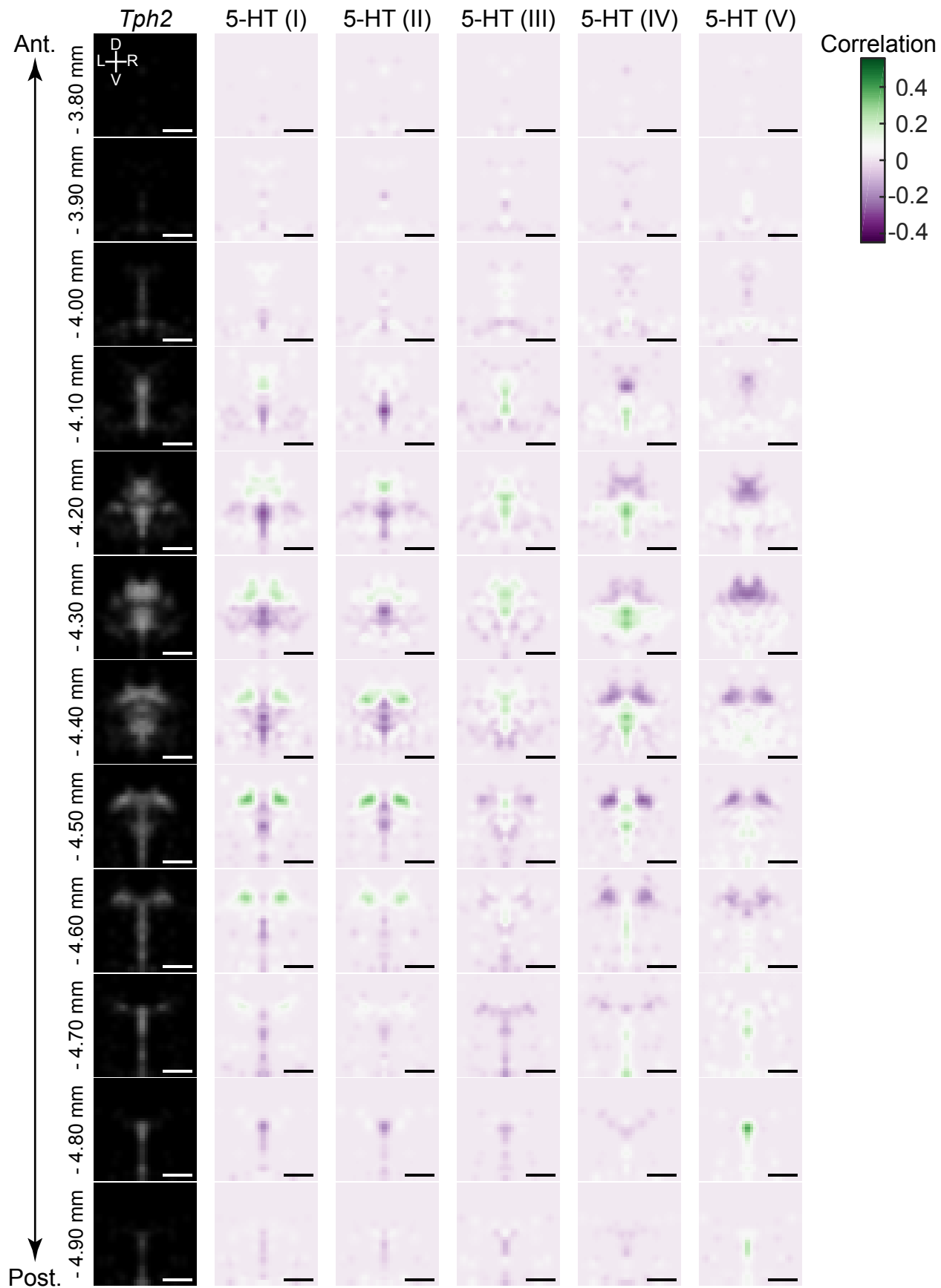


Figure S6

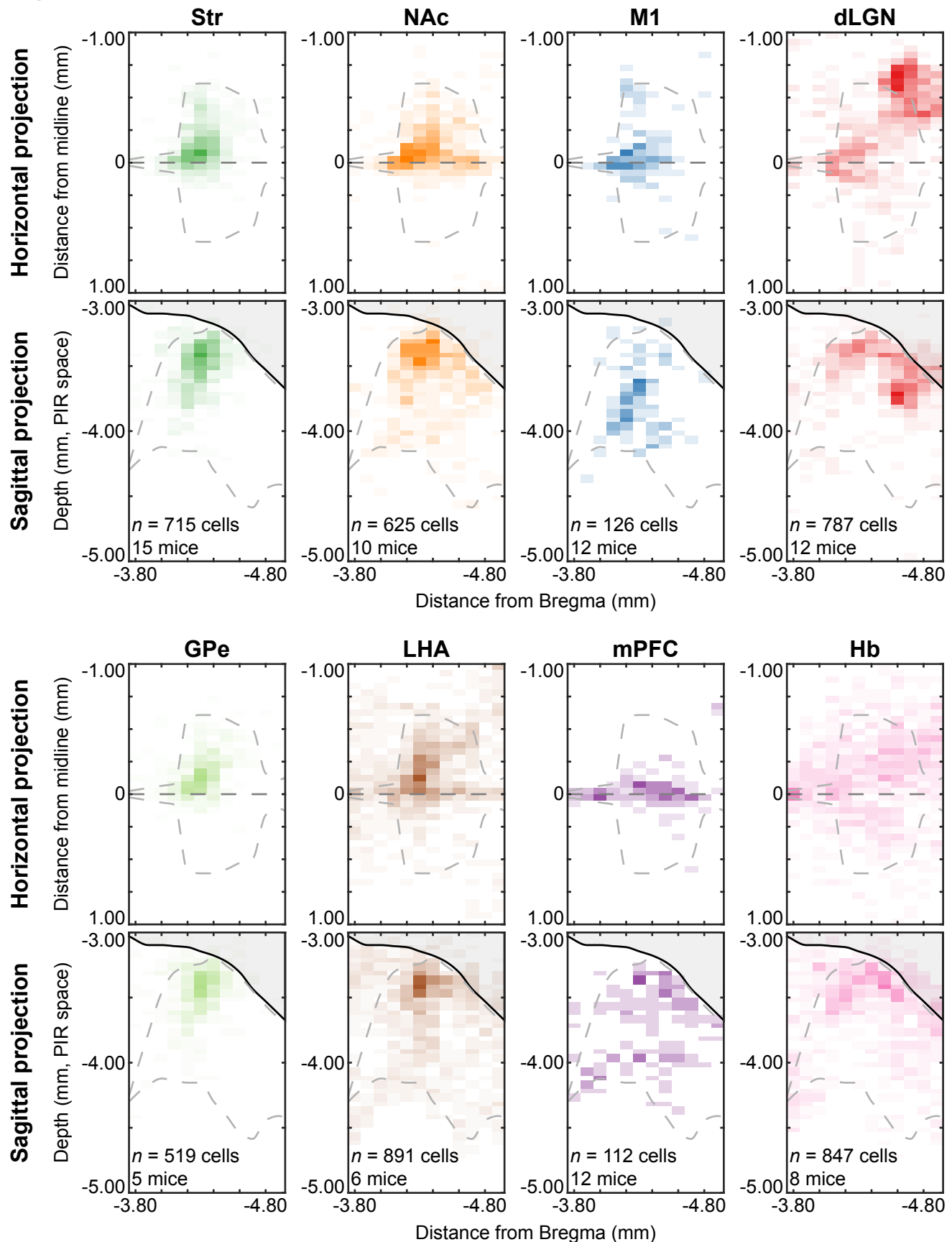


Figure S7

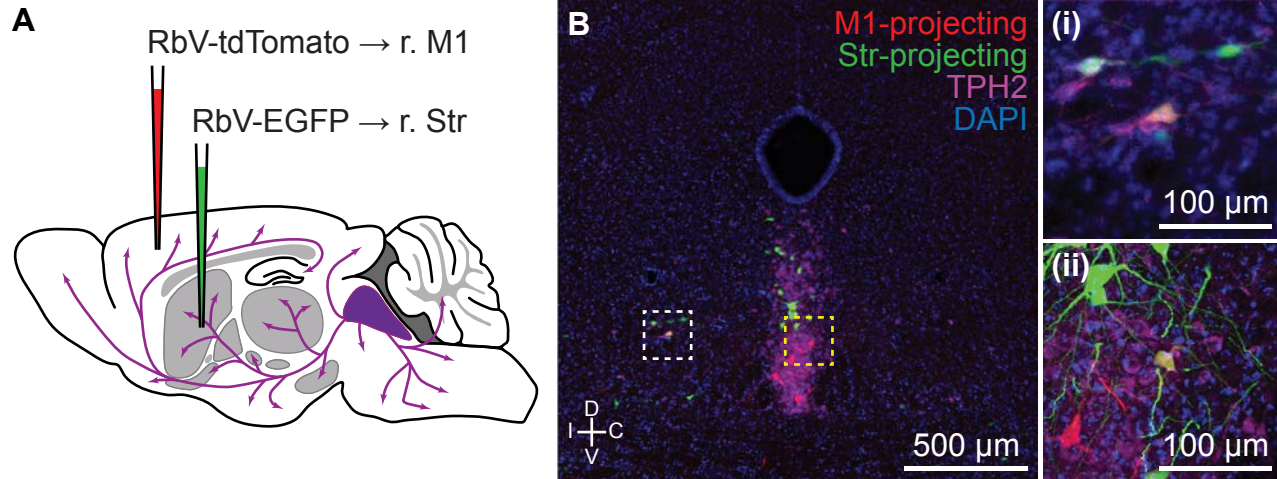


Figure S8

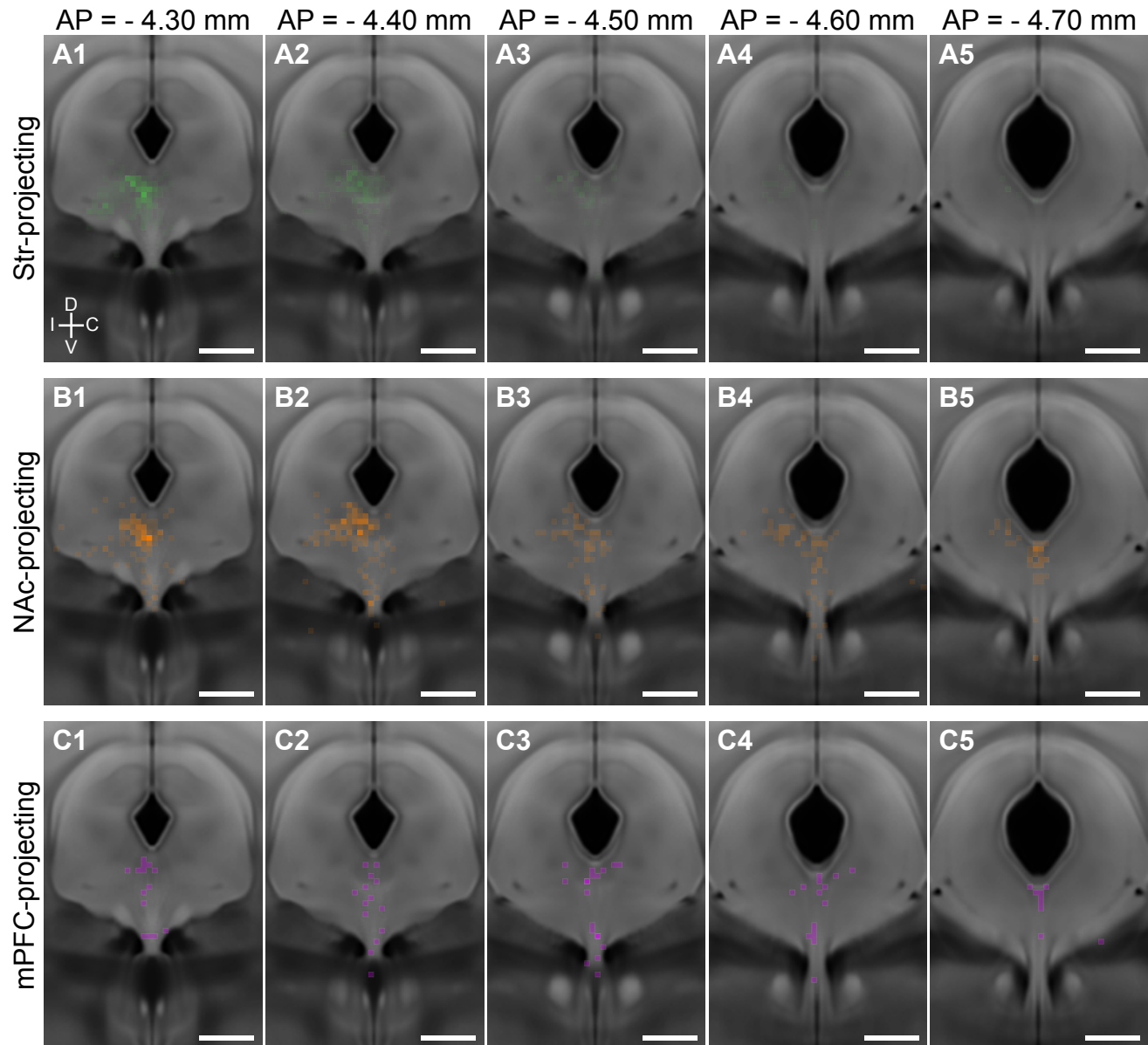


Figure S9

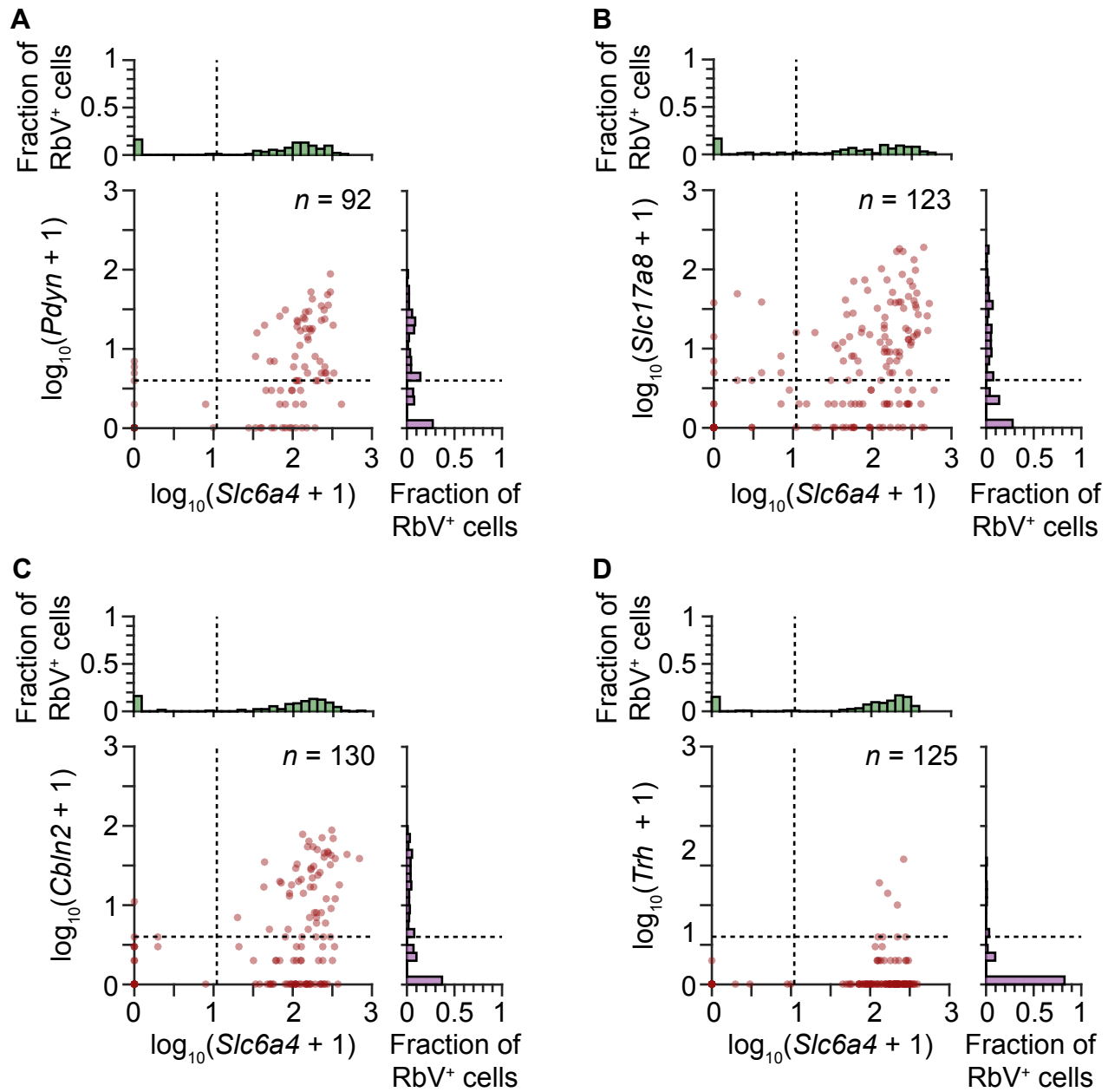


Figure S10

